THE UNIVERSITY OF QUEENSLAND
AUSTRALIA

CREATE CHANGE

SMP Poster Day 2020 Abstract Booklet

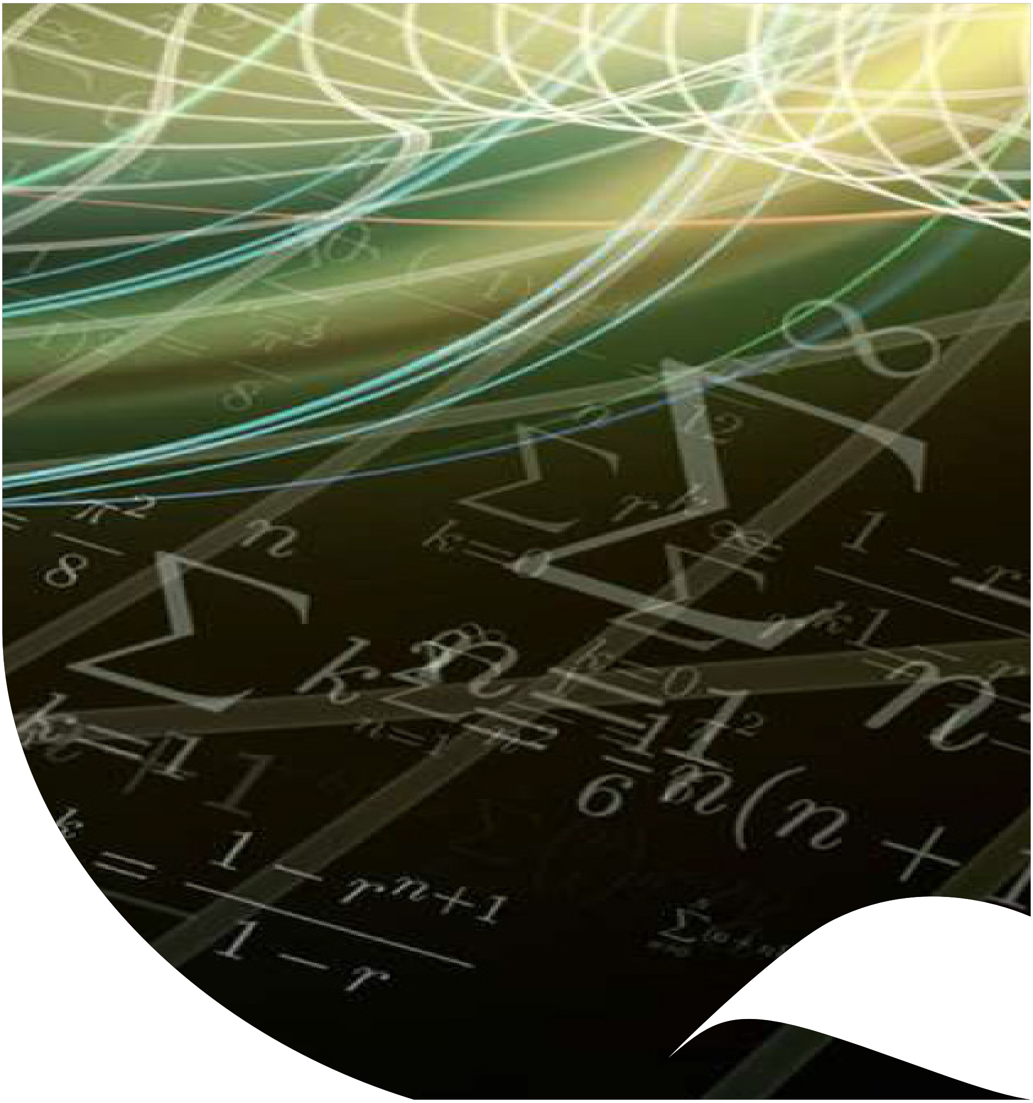

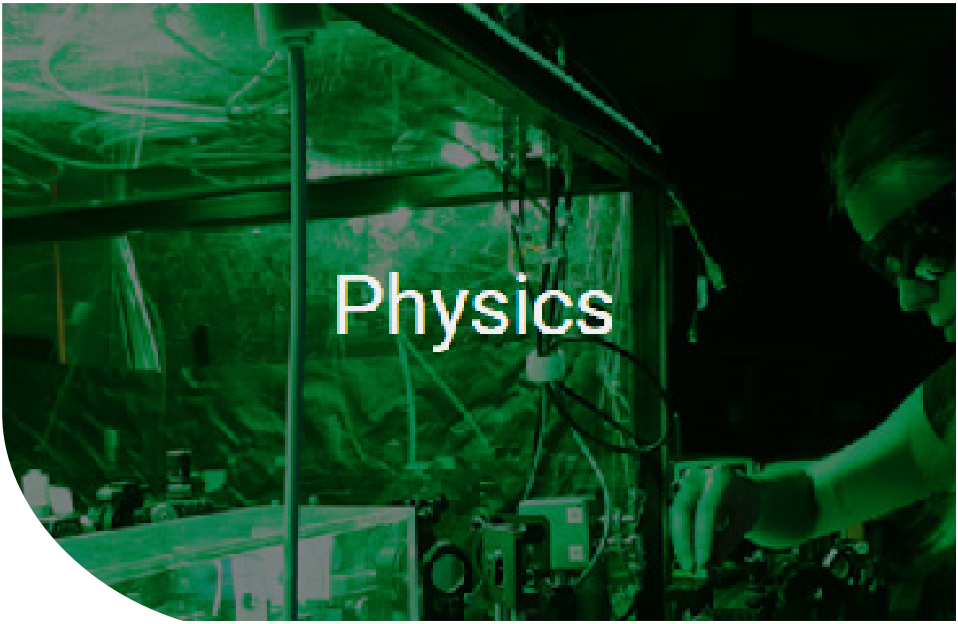
Physics

The "Cosmological Crisis"- Could it be Careless Corrections?

Aaron Glanville   Cullan Howlett   Tamara Davis

University of Queensland

The University Of Queensland Australia

A Crisis in Cosmology?

Our two key probes into expanding space (**standard candles**, and **standard rulers**) recover different values for the expansion rate of the universe (H_0).

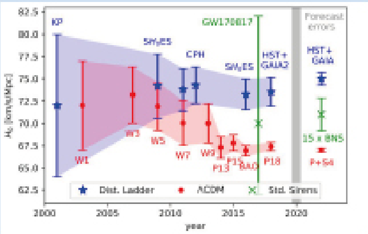

This discrepancy (~5-7 km/s/Mpc) has only grown in significance with improved precision [1]

Cosmic Structure as a "Standard Ruler"

"Standard Rulers" are cosmic structures of some known scale- We can trace expansion by measuring these structures over cosmic history!

Baryon Acoustic Oscillations (BAO) are a very powerful standard ruler- Shells of overdensity created by soundwaves in the early universe, which create a characteristic pattern in galaxy structure today [2]

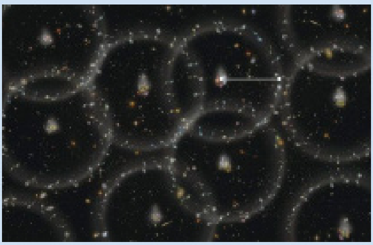

By measuring this scale today, we are measuring this yardstick after 13.8 billion years of expansion! We measure this echo as a series of wiggles in the galaxy matter power spectrum [3]:

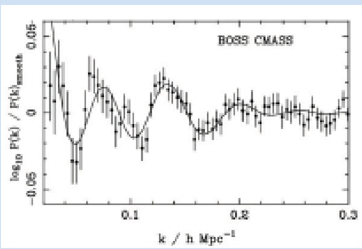

How do Errors Bias Standard Rulers?

When mapping cosmic structure, we can't measure galaxy distances directly- instead we rely on measurements of redshift (z) to infer distances,

$$D(z) = \frac{c}{H_0}\int_0^z \frac{dz}{\sqrt{\Omega_m(1+z)^3+\Omega_\Lambda}}$$

Redshifts probe the total line-of-sight velocity, but can't distinguish its source. When subtracting non-cosmological redshifts, common approximations can introduce sub-percentage redshift errors [4]- **How do these errors affect constraints in the era of precision cosmology?**

We test this by measuring the BAO feature in **500 mock surveys** (each with **~1,000,000 sources**), with and without injected redshift systematics

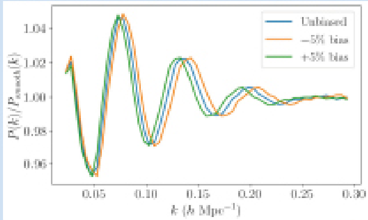

Redshift systematics dilate the peaks of the BAO feature, pushing this yardstick to different scales

We measure the average change in BAO scale under a range of conditions, and compare this to our theoretical model (dotted)

Our model very closely fits the observed shift in BAO scale, providing a reliable framework to predict and interpret how these errors will affect cosmological inference

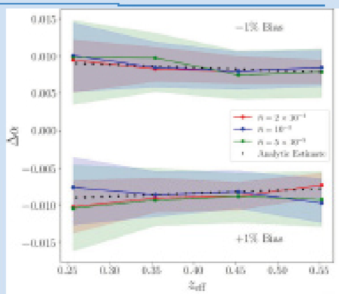

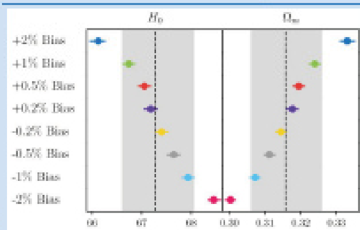

Using these mock surveys (with injected bias) to constrain cosmology, we find the **BAO feature is remarkably robust**: Sub-percentage biases yield only marginal (<0.5 km/s/Mpc) offsets in H_0, an order of magnitude smaller than our current tension

Conclusions

Cosmic standard rulers are remarkably robust to redshift errors. We show systematic redshift biases are very unlikely to bias cosmological parameters such as H_0, and develop a theoretical model to interpret and predict the impact of these systematics

Bibliography:

[1] Beaton et. al 2016 (arxiv: 1604.01788)
[2] Image by Zosia Rostomian, Lawrence Berkeley National Laboratories
[3] Anderson et. al 2012 (arxiv: 1203.6594)
[4] Davis et. al 2019 (arxiv: 1907.12639)

The “Cosmological Crisis”- Could it be Careless Corrections?

Aaron Glanville

Our two key probes into the nature of expanding space (standard candles and standard rulers) appear to disagree on the value of the present day expansion rate of the universe (H(0)). We explore the potential impact that previously negligible systematics could be playing in cosmological constraints provided by standard ruler measurements. We inject a series of systematics into 500 mock surveys (containing ~10^6 sources) and study how these systematics affect our cosmological rulers. We show plausible systematics are very unlikely to significantly contribute to this H(0) tension, and develop a theoretical model to interpret and predict the impact of these systematics.

Immiscible Spin Domains in a BEC

ALEXANDER PRITCHARD†, DAVID COLAS, THOMAS BELL, TYLER W. NEELY, HALINA RUBINSZTEIN-DUNLOP, & MARK BAKER

ARC Centre of Excellence for Engineered Quantum Systems (EQuS)
School of Mathematics and Physics, The University of Queensland, Brisbane, QLD, Australia 4075
†a.pritchard@uq.edu.au

THE UNIVERSITY OF QUEENSLAND
AUSTRALIA

1. SUMMARY

Bose-Einstein condensates (BEC) of dilute gases provide an excellent system for studying superfluid behaviours. Having condensates of various components constitutes multiple superfluids with different interaction strengths (different levels of miscibility). In our system we use this to study the stability/instabilities of a deterministic formation of a spin domain.

2. MULTI-COMPONENT BECS

A multi-component condensate is defined as having two or more internal quantum states that are macroscopically populated. For ^{87}Rb, the $F = 1$ atomic spin state can have three magnetic Zeeman substates $(2F+1)$, $m_F = -1, 0, +1$. Our experiment creates multi-component BECs using these substates. Having different substates effectively means you have multiple superfluids. This provides an extra degree of freedom allowing us to explore phenomena such as superfluidity, vortex formation and soliton behaviour. Imaging multi-component states can be done through Stern-Gerlach.

3. EXPERIMENTAL SETUP

The experiment uses a tightly focused, red detuned optical-dipole beam to trap our BEC, with condensate fractions of 70% and temperatures of 50nK. This forms a cigar shaped trap which provides tight radial confinement ($\omega_r \approx 2\pi \times 300$ Hz). A series of magnetic bias and gradient fields are used in combination with a well known RF pulse to perform varies state transfers to form a well localised domain. A spin-dependent optical barrier is also used to further localise the spin domain and can be controlled in space through a 2D AOD (See Figure below). Here we use a $F = 1, m_F = +1$ domain surrounded by $F = 1, m_F = -1$ state, which provides a nominally immiscible system given the relative s-wave scattering lengths.

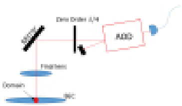

5. SPIN-DEPENDENT BARRIER

Optical BEC experiments usually use far detuned light to optically trap and cool atoms. For a mixed-species experiment this is either purely repulsive or attractive for all states. For ^{87}Rb a magic wavelength exists called the *tune-out wavelength*. This occurs when the blue detuning from the 795nm D1 line and red detuning from the D2 line cancel the dominant scalar ac Stark shift and we are left with the vector and tensor polarizabilities. These depend on the m_F state and light field polarization (given in parameters $C = A\cos(\theta_k)$ and $D = (3\cos^2(\theta_p) - 1/2)$)[1]. The figure to the right shows the ac Stark shift for Rb atoms in $m_F = 0$ (yellow/solid line), $m_F = +1$ (green/dashed) and $m_F = -1$ (blue/dot-dashed) ground states for $F = 1$.

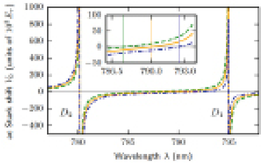

Plot is for right hand circularly polarised light (σ^+). The $m_F \pm 1$ states are shifted by more than 2nm apart. Figure taken from [1].

$$V^{(2)}_{nFm_F}(\lambda) = -\left(\frac{1}{2}E_0\right)^2 \left[\alpha^s_{nF}(\lambda) + C\frac{m_F}{2F}\alpha^v_{nF}(\lambda) - D\frac{3m_F^2 - F(F+1)}{2F(2F-1)}\alpha^T_{nF}(\lambda)\right] \quad (1)$$

6. RESULTS

Position stability of the formed domain at the centre of the trap (left plot) and a 50μm displacement of the domain using the barrier beam (right plot).

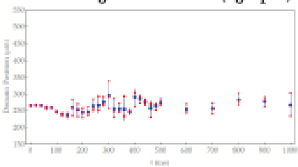

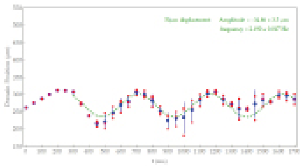

Furthermore, the bottom left table shows how the lifetime of the domain is affected by the condensate fraction/temperature (trapping frequency) and population fraction in the domain. Bottom right is a demonstration of how our protocol can be used to create multiple domains. Not shown here but the domains remain in their produced locations over time.

		Population Fraction		
		10%	15%	25%
ODT	222Hz/40%	0.31s	0.75s	1.11s
	234Hz/60Hz	0.24s	0.56s	1.02s
	249Hz/80Hz	0.14s	0.34s	0.41s

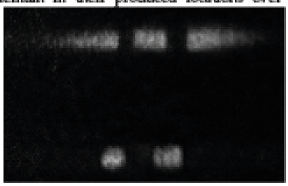

4. THE SEQUENCE

Time sequence of state creation (left figure), state after barrier is ramped off (center image) and with an applied gradient field after 50ms (right image). Imaging was down at 7ms time of flight using a Stern-Gerlach.

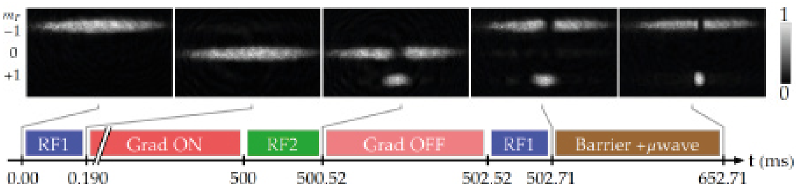

REFERENCES

[1] F. Schmidt, D. Mayer, M. Hohmann, T. Lausch, F. Kindermann, and A. Widera, "Precision measurement of the 87-rb tune-out wavelength in the hyperfine ground state f=1 at 790 nm,"

Engineering Spin Domains in a Binary BEC

Alexander Pritchard

The increased attention and development behind Bose-Einstein condensates (BECs) provides a system to study a wide range of phenomena to questions that haven't been answered to date. The extension to multi-component Bose-Einstein condensates, in various geometries, allows us to explore multiple BECs that interact different depending on their miscibility. With the use of Rabi pulses and magnetic bias fields we can change the internal magnetic hyperfine state of the atom to non-magnetically trappable states, which remain trapped in our optical dipole trap. Through this method, we can prepare two-component BECs of different hyperfine states. The interactions are dominated by the inter- and intra-species s-wave scattering. Depending on the choice of states, either a miscible or immiscible case can form. We explore an innovative way of trapping the spin states at a known location which can be further used for experiments.

Hunting Black Holes Mergers in Star Clusters

A. D. Arnold & Holger Baumgardt
anthony.arnold@uqconnect.edu.au
School of Mathematics and Physics, The University of Queensland

The University of Queensland
Australia

Black Hole Mergers

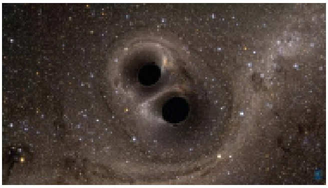

Artist's impression courtesy of www.black-holes.org

- When black holes meet they spiral towards each other, emitting energy in the form of gravitational waves.
- There have been dozens of recorded black hole mergers from the LIGO and Virgo observatories since 2015.

But How?

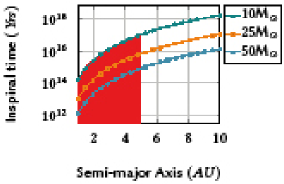

- Isolated stars can't become black holes and then merge.
- The inspiral time is greater than the age of the universe!
- Something else must be driving them together.

Globular Clusters

- Systems of 10^5 to 10^7 stars tightly bound by gravity.
- Produce exotic phenomena:
  - Millisecond pulsars
  - Black holes
- Dense and dynamic enough to make black hole mergers possible.

Gravitational N-body Simulation

- Gravitational N-body simulations of dense stellar systems like star clusters are resource intensive activities.
- Direct-N schemes, where every particle interacts with every other particle, require n^2 interactions per time step.

- Simulations take months or years to complete.

Our Strategy

- Modify NBODY6, the state of the art in gravitational n-body simulation.
- Replace the distant force calculator with a tree code.
- Integrate distant forces with a leap frog scheme.

Distant vs. Near Forces

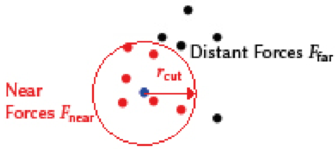

The Tree Code - A Fast Approximation

- Recursively sub-divide the space, forming a tree.
- Starting at the top node, check:
  - If the node is sufficiently distant, approximate the gravitational force using the node's centre of mass.
  - Otherwise, visit each child node and apply the same check.

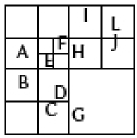

Integration Scheme

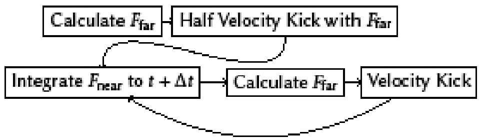

Results

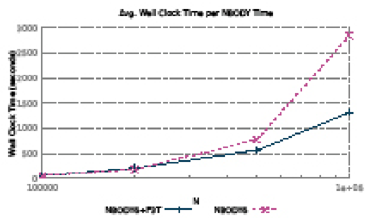

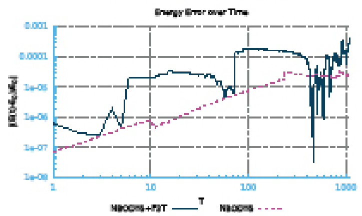

Hunting Black Hole Mergers in Star Clusters

Anthony Arnold

When black holes merge, they release enormous amounts of energy in the form of gravitational waves. But how can two black holes form and then merge? One possibility is that they form inside globular clusters, which are highly dynamic and gravitationally bound. However, these clusters are huge; they can contain millions of stars and take a lot of effort to integrate their evolution over time scales as long as 15 billion years. We made some modifications to existing simulation software to make this job easier. By introducing a faster, albeit approximate, algorithm for calculating gravity we were able to reduce the simulation execution time by half.

Can age-old approximations bias Cosmology?

A mystery of cosmological proportions

Anthony Carr, Tamara Davis and Daniel Scolnic

The Suspect: Heliocentric Corrections

- Redshifts (z) are fundamental to Cosmology due to the expansion of the universe.
- We fit Cosmological parameters using redshifts in the global rest frame (the rest frame of the cosmic microwave background, CMB).
- The Solar System's own velocity must be factored out of observed redshifts.
- Using supernovae as standard candles, we compare apparent brightness to redshift to probe the universe's expansion history.
- Surprisingly small systematic biases in z (x-axis) bias Cosmology if at low-z.

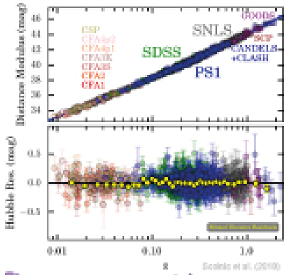

The correct way to add redshifts is in factors of (1+z):

$$1 + z_{\rm obs} = (1 + z_{\rm CMB})(1 + z_{\rm Sol}).$$

However we often see this approximated as

$$z_{\rm obs} = z_{\rm CMB} + z_{\rm Sol},$$

which is accurate at low-z, but has error that scales as $z_{\rm CMB} z_{\rm Sol}$.

This is a *systematic* error, but depends on sky position:

$$z_{\rm Sol} \approx \frac{v_{\rm Sol}}{c} \cos\alpha,$$

Where α is angular separation from the CMB dipole.

The Evidence: The NASA Extragalactic Database

- Using ~200,000 galaxies from the leading astrophysical database (NED for short), we demonstrate the approximation is being used.
- We compute the full heliocentric-corrected redshifts $z^{\times}_{\rm CMB}$ and compare to those given by NED, $z^{\rm NED}_{\rm CMB}$.
- The sinusoid in α and linearity with $z^{\times}_{\rm CMB}$ confirm our suspicions.

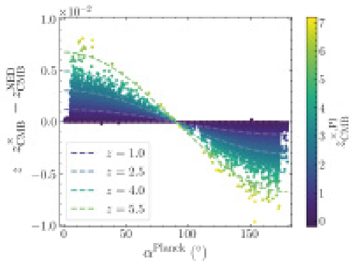

- We also confirm NED uses the outdated Cosmic Background Explorer measurement of the CMB dipole (Fixsen et al. 1996) instead of the Planck 2018 measurement.

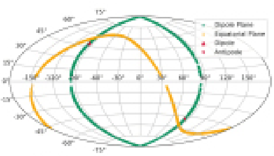

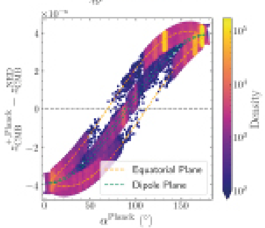

With the two distinct regions of galaxies, we detect the slight change in $z_{\rm CMB}$ caused by the dipole shift.

We can accurately model the exact effects we expect (dashed lines).

The excellent agreement between theory and data again confirms our suspicions.

We are now collaborating with the NED team to use the full correction and update the dipole.

The Evidence: In the Pantheon Supernova Sample

- The approximation is also present in the current leading supernova sample, the 'Pantheon' sample.
- When we compare our computed correction with redshifts in Pantheon we see exactly the same behaviour as in NED.

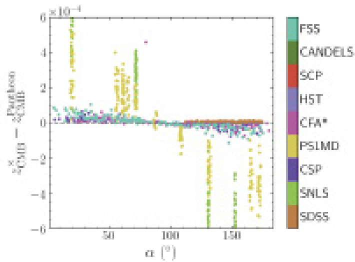

- The highly anisotropic 'pencil beams' (vertical lines in figure) often used for supernova monitoring are the most vulnerable to the approximation.
- We are also working with the Pantheon team to use the full correction, as well as completely overhaul the redshifts for the whole sample.

The Verdict

The question remains: can an approximated heliocentric correction bias cosmology? Yes. Does it? The investigation is still ongoing, but preliminary analyses show only negligible bias.

Fortuitously, Pantheon equally covers all-sky, so the large errors we see mostly cancel.

However, this is still an important issue, as the Dark Energy Survey supernova sample will be at least double the size of Pantheon and highly anisotropic.

References

Scolnic, D. M., Jones, D. O., Rest, A., et al. 2018, ApJ,859, 101

Fixsen, D. J., Cheng, E. S., Gales, J. M., et al. 1996, ApJ,473, 576

Planck Collaboration, Aghanim, N., Akrami, Y., et al.2020, A&A, 641, A1

Can age-old approximations bias Cosmology?

Anthony Carr

One of the most pressing issues in Cosmology today is the disagreement in the expansion rate of the universe as measured locally using supernovae, and as inferred from the Cosmic Microwave Background. We must now turn our attention to as-yet unaccounted for systematics in our local measurements. One such systematic arises from the heliocentric correction to our redshifts, that is often approximated. Through my research, I show that this approximation is still being used in the leading astrophysical database and, as well as the leading supernova sample. I then show how this approximation can bias the local supernovae measurements.

Constraining Vector Mediated Dark Matter in GAMBIT

Christopher Chang, Supervisor: Dr Pat Scott

Vector Mediated Fermion Dark Matter

This model adds two new particles not present in the Standard Model: a vector boson, V_μ, and a dirac fermion dark matter candidate, χ. The Lagrangian that describes this behaviour is:

$$\mathcal{L} \supset g_\chi V_\mu \bar{\chi} \gamma^\mu + \sum_q g_q V_\mu \bar{q} \gamma^\mu q$$

And the free parameters in this model are the coupling constants and the masses of each particle:

$$[g_\chi, g_q, m_\chi, m_{V_\mu}]$$

This is more easily visualised with the lowest order tree-level Feynman diagram:

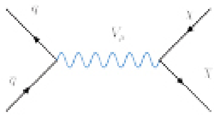

V_μ interactions exchanges between quarks and χ (and its antiparticle). This model lies in a class of models (simplified models) that are not required to be renormalizable or well described at higher energy scales. Instead, the existence of this behaviour would require further particles or interactions in order for the theory to be gauge invariant and UV complete. The aim of these models is to inform the phenomenology of larger encompassing theories.

Jet Matching

In order to use the ColliderBit module [2] in GAMBIT confidently with new models, we had to adopt a Jet Matching scheme. Optimally, the method would be to generate events at the matrix element level in MadGraph [3], and pass these to Pythia [4] for parton showering. Appropriate cuts would then be performed at both levels to reject non-matched parton jets between the two (method is referred to "MLM" matching). In order to avoid generating events in both MadGraph and Pythia, we have opted to generate events solely with Pythia, and approximate the MLM matching using Pythia's inbuilt matching framework along with appropriate phase space cuts. The accuracy of my implementation of this approximation can be judged by comparing the simulated jet transverse momentum distribution:

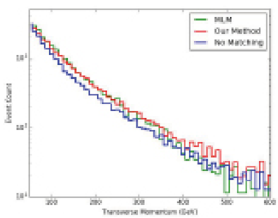

Our method of jet matching appears to agree with MLM well in the low transverse momentum, high event count regions.

Dark Matter Constraints

I performed a dark matter scan with DarkBit [1], applying relic abundance, indirect detection and direct detection constraints. All four free parameters were varied, with the different couplings marginalised over to produce constraints on the mass of the new particles.

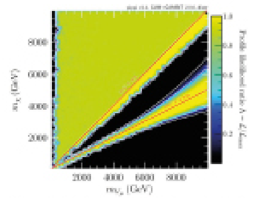

The dominant observable affecting the likelihood was the relic abundance. The region above the $m_\chi = m_{V_\mu}$ boundary is allowed as $\chi\chi$ can decay to $V_\mu V_\mu$. At $m_{V_\mu} = 2m_\chi$, the excess dark matter above the observed relic density can be avoided as V_μ is on resonance. Annihilation of χ into Standard Model particles via exchange of a V_μ causes a distinct diagonal high likelihood region. In the region below the $m_\chi = m_{V_\mu}$ boundary, as decay into V_μ becomes off-shell, the increased thermally produced dark matter can longer annihilate as efficiently. This causes a rise in the relic density of dark matter to the point where it exceeds the observations from cosmology

Collider Simulation

In order to validate the Collider machinery for this model, I scanned over varying masses but with fixed couplings. The likelihood was based on a CMS mono-jet analysis at the LHC [5] with a high degree of missing detected energy from χ.

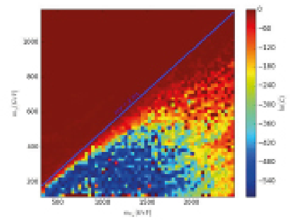

A low dark matter mass relative to the mediator mass causes this decay into χ to be significant. Given the expected signal from this, the lack of evident excesses in the LHC data rules out large regions of this parameter space. This is the cause of the dramatically low collider likelihoods for low mass mediators and suggests that the energy scale of the mediating process would be high enough to be well described by effective field theories.

What's next?

In order to run full scans with the collider likelihoods (to combine with dark matter likelihoods and produce global fits), further development of the collider machinery is needed. Narrow features in the spectrum cause poor phase space sampling by the Monte Carlo generator, drastically increasing the computation time. With smarter phase space sampling, I will scan the full model parameter space, producing constraints on the model as a whole.

[1] The GAMBIT dark matter working group, 2017, DarkBit European Physical Journal C, 77, 831.
[2] The GAMBIT collider working group, 2017, ColliderBit, European Physical Journal C 77, 795
[3] Alwall, J. et al. 2011, MadGraph 5: going beyond, Journal of High Energy Physics 2011.
[4] Sjöstrand et al, 2008, A brief introduction to PYTHIA 8.1, Computer Physics Communications 178, 852-867.
[5] Sirunyan, A.–M. et al, 2018, Search for new physics in final states with an energetic jet or a hadronically decaying W or Z boson and transverse momentum imbalance at sqrt(s)=13 TeV, Physical Review D 97

Constraining Vector Mediated Dark Matter in GAMBIT

Christopher Chang

Extensions to the Standard Model offer a strong theoretical framework to describe dark matter. The lack of an unambiguous detection of new particles therefore constrains the parameter space of new theories. My work has been to add one of these theories into the GAMBIT pipeline to perform global fits of a simplified dark matter model. This adds a dark matter fermion and a spin-1 boson to mediate exchanges to Standard Model particles. In order to do this, GAMBIT's collider module must first be upgraded to accommodate a wider range of particle theories. Having now adapted the machinery to allow parton jet matching, smarter phase space sampling is the last step before full global fits will be performed. As most studies of simple extensions to the Standard Model only explore a subset of the parameter space, full fits will help to inform future particle searches.

Constraining the fundamental number of quantum degrees of freedom using gravity

Harshit Verma, Magdalena Zych, Fabio Costa

h.verma@uq.edu.au

Centre for engineered quantum systems (EQUS), School of Mathematics and Physics, University of Queensland, St Lucia 4072, QLD, Australia
School of Mathematics and Physics, University of Queensland, St Lucia 4072, QLD, Australia

THE UNIVERSITY OF QUEENSLAND AUSTRALIA
CREATE CHANGE
EQUS

INTRODUCTION

- Question: How many fundamental particles are present in the universe?
- Approach:
  - Fundamental particles in the universe are quantization of fundamental fields.
  - Fundamental fields can be visualized as many interacting quantum DOF.
- Background: Probe gravitational effects in quantum systems in the low energy regime.
- Refined question: Can we devise an experiment in the low energy regime to constrain the number of quantum DOF?
- Theoretical framework: Gravitational redshift and gravitational decoherence due to time dilation.

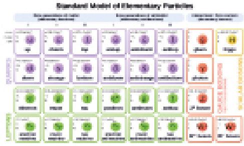

GRAVITATIONAL RED SHIFT IN EXTENDED QUANTUM SYSTEMS WITH INTERNAL DOF AND DECOHERENCE

MOTIVATION

Experimentally testable

Near term simulation on quantum hardware

Toy model for fields

E.g. spin chain systems

Sum of Local Hamiltonians

$H_0 = \sum_{i=1}^{L} h_i$

(A) DIFFERENTIAL REDSHIFT

1D extended quantum system

Redshift profiles (indicative only)

PARTS OF THE TOTAL HAMILTONIAN

$H = H_{cm} + H_0 + H_{int}$

H_{cm} = trivial $\quad H_0 = \sum_{i=1}^{L} h_i \quad H_{int} = \sum_{i=1}^{L} h_i\,\phi(r_i)$

(B) GEDANKEN EXPERIMENT

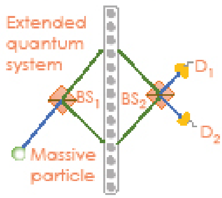

- Scenario: Extended quantum system with internal DOF, with a massive particle nearby.
- Assumption: T = 0, massive particle is brought adiabatically near the system.
- (A) Total Hamiltonian (hence, the ground state) depends on the redshift profile - the relative position of mass from the spin chain.
- (B) If mass is prepared in a spatial superposition, the ground state of spin chain is entangled with the position of mass: $|\Psi\rangle = |R_1\rangle\,|GS\rangle_{R_1} + |R_2\rangle\,|GS\rangle_{R_2}$

Entangled state due to differential redshift → Trace out the internal DOF → Measure the COM in ± basis → **Decoherence !**

$M = |\langle GS_{R_2}|GS_{R_1}\rangle|$

Visibility of path DOF

- Inference: **Low visibility** → **Low overlap b/w GS** → **High decoherence**

DECOHERENCE IN SPATIAL SUPERPOSITION OF MASSIVE PARTICLE DUE TO SPIN CHAINS

MODELLING DIFFERENTIAL REDSHIFT IN SPIN CHAINS

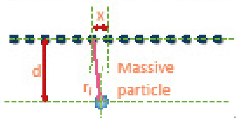

Red shift factor :

$$\sqrt{-g_{00}} \approx \sqrt{1+2\phi(\vec{r}_i)} \approx (1+\phi(\vec{r}_i)) \qquad \phi(\vec{r}_i) = -G\frac{M}{|\vec{r}_i|}$$

$$r_i = \sqrt{\left((k-i)+\frac{1}{2}\right)x^2 + d^2} \quad \forall i \in [1, L],\ \text{for } \phi_i$$

$$r_i = \sqrt{(k-i)x^2 + d^2} \quad \forall i \in [1, L-1],\ \text{for } \phi_{i,i+1}$$

Original Hamiltonian : $H = J_x \sum_{i=1}^{L-1}\left(S_i^x S_{i+1}^x + S_i^y S_{i+1}^y\right) + J_z \sum_{i=1}^{L-1} S_i^z S_{i+1}^z - \sum_{i=1}^{L} B_i S_i^z$

Red shifted Hamiltonian : $H = J_x \sum_{i=1}^{L-1}(1+\phi_{i,i+1})\left(S_i^x S_{i+1}^x + S_i^y S_{i+1}^y\right) + J_z \sum_{i=1}^{L-1}(1+\phi_{i,i+1}) S_i^z S_{i+1}^z - \sum_{i=1}^{L}(1+\phi_i) B_i S_i^z$

RESULTS

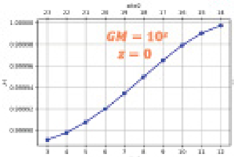

XXZ chain : $J_x = J_z = B = 1$

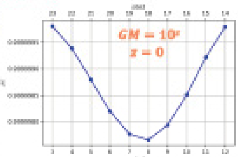

XX chain : $J_x = 1, J_z = B = 0$

CONSTRAINING THE NUMBER OF QUANTUM DOF

LIMITING CASE WITH SCHWARZCHILD BLACK HOLE

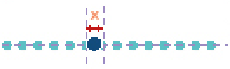

Red shift factor : $\sqrt{-g_{00}} = \sqrt{1 - \frac{r_s}{2r_i}}$

$r_i = |(k - i + 1/2)|\,r_s$

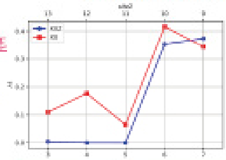

REFERENCES

[1] Pikovski I., Zych M., Costa F., and Brukner C., Universal decoherence due to gravitational time dilation, Nature Physics, 11, 668 (2015).

- N number of spin chains lying at the same relative position wrt. the massive particle.
- Each contributes equally to the decoherence : $M^N \to 0$.
- Limit α arbitrarily close to 0, defined by the limit of experimental observation. $M^N \to e^{-\alpha}$, $N = -\alpha/\ln(M)$

FOR BH:

$N = 2$ for $\alpha = 2$

FOR FINITE MASS :

$N = 10000$ for $\alpha = 2$, $\ln z = 0$, XXZ

Constraining the fundamental number of quantum DOF using gravity

Harshit Verma

How many quantum degrees of freedom (DOF) are present in the universe is a fundamental open question in Physics. I will discuss how gravity can be used to approach this important question, elaborating on the interplay between quantum mechanics and gravity in the process. This quest is grounded in a series of recent works focusing on the low energy regime, which explore the effect of gravity on quantum systems manifesting as time dilation of an evolving quantum DOF. I will introduce the phenomenon of gravitational decoherence of a spatial superposition arising in this formalism and widen its scope to include extended quantum systems (EQS) while highlighting the key differences this exercise entails. Finally, using spin chain as a toy model for EQS, I will present the number of independent EQS which can cause reasonable decoherence in the spatial superposition of the massive particle. The coherence observed in an actual experiment can therefore, be used to put a fundamental limit on the number of quantum DOF surrounding the spatial superposition of a massive particle, thus answering the aforementioned open question.

Schrödinger's cat for de Sitter spacetime

Motivations

- Quantum gravity ⇔ descriptions of **spacetime in quantum superpositions**.
- **New phenomenological description** of a metric in a superposition of curvatures, **using an Unruh-deWitt (UdW) detector**.
- **Scenario 1:** static detector in a superposition of spacetime locations ⇔ spacetime in a superposition of translations.
- **Scenario 2:** static detector on a background metric in superposition of curvature ≠ classical analogue!

UdW formalism

- UdW detector ⇒ two-level system coupled to **control DoF in superposition**, interacts with quantum fields:

$$|\Psi\rangle_{\text{cfd}} = \underbrace{\frac{1}{\sqrt{N}}\sum_{i=1}^{N}|c_i\rangle}_{\text{control}} \otimes \underbrace{|g\rangle}_{\text{UdW}} \otimes \underbrace{|0_{\text{dS}}\rangle}_{\text{dS vacuum}} \qquad (1)$$

with interaction Hamiltonian

$$\hat{H}_{\text{int.}} = \lambda\hat{\sigma}(\tau)\sum_{i=1}^{N}\eta(\tau)\hat{\Phi}(\mathsf{x}_i(\tau))\otimes|c_i\rangle\langle c_i| \qquad (2)$$

- To leading order in perturbation theory, the detector response (transition probability) is

$$\mathcal{F} = \frac{\lambda^2}{N^2}\sum_{i,j=1}^{N}\int \mathrm{d}s\, e^{-s^2/4\sigma^2}e^{-i\Omega s}\mathcal{W}^{ij}(s), \qquad (3)$$

where $\mathcal{W}^{ij}(s) = \langle 0_{\text{dS}}|\hat{\Phi}(\mathsf{x}_i)\hat{\Phi}(\mathsf{x}_j)|0_{\text{dS}}\rangle$.
- Inclusion of control DoF allows us to define the fields along **different paths in superposition**, or even **different background metrics**.

Detector response in de Sitter

- Static de Sitter (dS) metric:

$$\mathrm{d}s^2 = -(1 - a^2R^2)\mathrm{d}T^2 + \frac{\mathrm{d}R^2}{1 - a^2R^2} + R^2\mathrm{d}\Theta^2 \qquad (4)$$

where $a =$ dS length, $\mathrm{d}\Theta^2 = \mathrm{d}\theta^2 + \sin^2\theta\,\mathrm{d}\phi^2$.

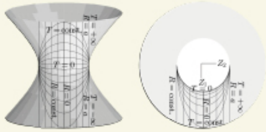

Figure: dS hyperboloid where $a^2 \propto \Lambda$ (cosmological constant).

- A detector on a classical path:

$$\mathcal{F} \propto \frac{1}{e^{2\pi\Omega/\kappa} - 1} \qquad (5)$$

where $\kappa = 1/\sqrt{a^{-2} - r^2}$ i.e. thermal response.
- Detector in superposition of coordinates $(\mathsf{x}, \mathsf{x} + \mathcal{L})$:

$$\mathcal{F} \propto \frac{1}{e^{2\pi\Omega/\kappa} - 1}\left[1 + \frac{\sin\left(2\Omega\kappa^{-1}\sinh^{-1}(\mathcal{L}\kappa/2)\right)}{\mathcal{L}\Omega\sqrt{1 + (\mathcal{L}\kappa/2)^2}}\right] \qquad (6)$$

i.e. $\mathcal{F}(\Omega)/\mathcal{F}(-\Omega) = \exp(2\pi\Omega/\kappa) =$ thermal!

Diffeomorphic invariance

- Metric 'felt' by the **detector traveling in superposition of coordinates**: diffeomorphic to **detector on a classical worldline with spacetime in a superposition of translations**.
- Observables (e.g. $\mathcal{F}$) are **invariant under this global transformation** between perspectives (quantum reference frames).

Superpositions of curvature

- Can define $\mathcal{W}^{ij}(s)$ (Eq. 3) w.r.t fields $\hat{\Phi}(\mathsf{x}_i)$, $\hat{\Phi}(\mathsf{x}_j)$ quantised on dS metrics with **different** values of spacetime curvature (i.e. $a_1 \neq a_2$)
- Metric in superposition of curvatures ⇎ single metric with 'classical' dS length. Beyond semi-classical description!
- **Superposition of a's in dS ⇔ superposition of proper accelerations in flat Minkowski spacetime.**

The anti-Gibbons-Hawking effect

- For detector in superposition of $(\mathsf{x}, \mathsf{x} + \mathcal{L})$ with finite-time interactions ⇒ anti-Gibbons-Hawking behaviour.
- **Detects fewer quanta as the field temperature increases!** Connection to quantum information ⇒ coherent superposition of (thermal) channels.

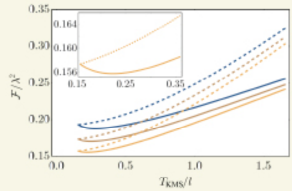

Figure: Response function, $\mathcal{F}$, as a function of the field temperature, T_{KMS}, for (dashed) classical paths and (solid) detectors in superposition.

Joshua Foo, Robert B. Mann & Magdalena Zych
jfoobles@gmail.com
School of Mathematics and Physics, University of Queensland

Schrodinger's cat for de Sitter spacetime

Joshua Foo

A self-consistent theory of quantum gravity is expected to contain descriptions of classical spacetime geometries in quantum superpositions. Here, we provide a new phenomenological description of a metric in a superposition of curvatures, using an Unruh-deWitt detector. The detector interacts with the conformally coupled vacuum state defined on a static de Sitter metric in a superposition of curvatures. The instantaneous transition rate of the detector has a direct correspondence with that of a detector travelling in a superposition of proper accelerations in Minkowski spacetime. We also study the detector in a superposition of spatial translations, discovering that its response is thermal and likewise corresponds with that of a detector in a superposition of spatially translated accelerated trajectories in Minkowski spacetime. For such detectors, we demonstrate the emergence of so-called anti-Gibbons-Hawking behaviour, which would be otherwise absent for detectors travelling on classical trajectories.

Interfering Two Photons Irrespective of Their Location

Joshua J. Guanzon, Austin P. Lund, and Timothy C. Ralph.

UQ

CQC2T

Our Research Problem Explained

Two photons, injected into a beam splitter, experiences quantum interference.

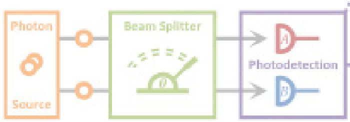

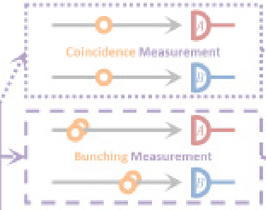

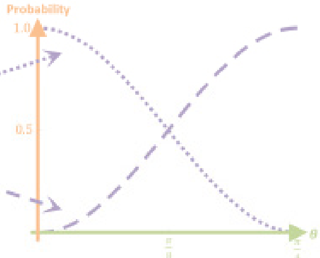

Imagine a photon source which randomly injects two photons into m input ports.

What we discovered is an optical circuit which can accept any of these inputs...

...and generate the same photon number statistics of a beam splitter.

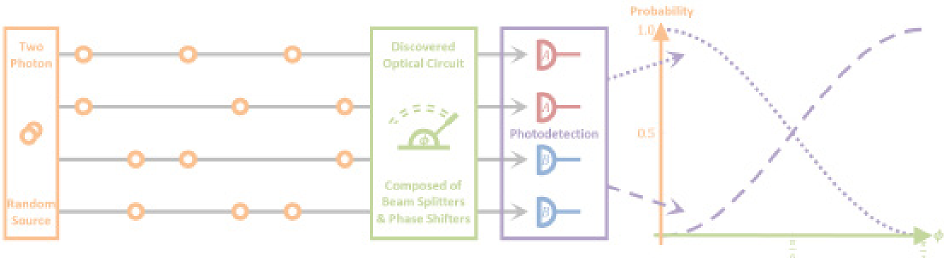

Motivation

1. Beam splitters are the basic building blocks for many optical circuits. With phase shifters, any unitary transformation can be done.

2. Sampling advantage since we can disregard location. This advantage increases with m.

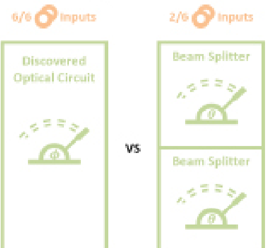

Applications and Future Direction

1. Confirming photon pair indistinguishability can be done by looking at the destructive interference of coincidence counts. Our circuit can do this for multiple photon sources/pairs simultaneously.

2. Verification of configurable circuits since the probability of observing certain measurement outcomes are known with our circuit.

3. Quantum metrology is possible as we can decompose our circuit into a form which allows phase estimation. The Fisher information appears to be input location invariant, for all possible photon inputs. This will be investigated in the future.

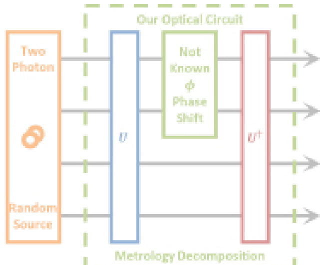

Reference

Guanzon, J. J., Lund, A. P., & Ralph, T. C. (2020). Controllable quantum interference from two-photon scattershot sources. Physical Review A, 102(3), 032606.

Interfering Two Photons Irrespective of Their Location

Joshua Guanzon

We describe a multimode passive optical circuit which can emulate the two-photon number statistics of a beam splitter, irrespective of where the two photons entered the optical circuit [1]. These photon number statistics includes the absence of coincidence counts (i.e., the Hong-Ou-Mandel dip), a 100% coincidence rate, as well as all possible two-photon beam splitter statistics between these two extremal points. The input location invariance property means it can take advantage of certain types of single-photon sources to have enhanced sampling rates, whose advantage scales with larger circuit sizes. We will also present very recent results (not covered in our paper [1]), in which we show that these optical circuits can also be used for quantum metrology with interesting information symmetry properties.

References [1] Guanzon, J. J., Lund, A. P., & Ralph, T. C. (2020). Controllable quantum interference from two-photon scattershot sources. Physical Review A, 102(3), 032606.

Symmetry Breaking Equilibria in a Quantum Vortex Gas

Matthew T. Reeves,[1] Kwan Goddard-Lee,[2] Guillaume Gauthier,[2] Oliver R. Stockdale,[1] Hayder Salman,[3] Timothy Edmonds,[1] Xiaoquan Yu,[4,5] Ashton S. Bradley,[5] Mark Baker,[2] Halina Rubinsztein-Dunlop,[2] Matthew J. Davis,[1] and Tyler W. Neely,[2]
[1]Australian Research Council Centre of Excellence in Future Low-Energy Electronics Technologies (FLEET), University of Queensland
[2]ARC Centre of Excellence for Engineered Quantum Systems (EQuS), University of Queensland
[3]School of Mathematics, University of East Anglia
[4]Graduate School of China Academy of Engineering Physics
[5]Department of Physics, Centre for Quantum Science, and Dodd-Walls Centre for Photonic and Quantum Technologies, University of Otago
Website: http://www.equs.org/ Email: kwan.goddardlee@gmail.com

Overview

Bose Einstein Condensates (BECs) behave as nearly ideal fluids, allowing many previously inaccessible fluid dynamic phenomena to be experimentally observed and explored. In particular we are interested in the behaviour of quantised vortices which, in two dimensions, tend to cluster together at high energy. This is an equilibrium state known as an Onsager Cluster.

BEC Experiment and Methods

The experimental apparatus at UQ facilitates highly controllable and repeatable experiments on BECs tightly confined vertically. Using a Digital Micromirror Device (DMD) we can confine the BEC in an arbitrary two dimensional potential. This gives a very high degree of dynamic control over the BEC allowing many experiments, including two-dimensional fluid dynamics, to be conducted [4].

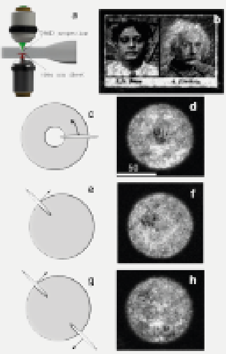

Fig. 1 - Using 532 nm light controlled by the DMD a) we can create arbitrary potentials in the BEC, for example portraits of Bose and Einstein b). We can also create "paddles" to stir the condensate and create vortices in various initial positions with sequences c) e) and g). These sequences create on-axis (d) and off-axis (f) vortex clusters as well as two symmetrically placed clusters (h) respectively.

References

[1] R. A. Smith and T. M. O'Neil, "Nonaxisymmetric thermal equilibria of a cylindrically bounded guiding-center plasma or discrete vortex system", Phys. Fluids B 2, 2961 (1990)

[2] L. Onsager, "Statistical hydrodynamics," Il Nuovo Cimento (1943-1954), vol. 6, pp. 279-287, 1949.

[3] X. Yu, T. P. Billam, J. Nian, M. T. Reeves, and A. S. Bradley, "Theory of the vortex-clustering transition in a confined two-dimensional quantum fluid" Phys. Rev. A 94, 023602 (2016).

[4] G. Gauthier, I. Lenton, N. McKay Parry, M. Baker, M. J. Davis, H. Rubinsztein-Dunlop, and T. W. Neely, "Direct imaging of a digital-micromirror device for configurable microscopic optical potentials," Optica 3, 1136-1143 (2016)

[5] G. Gauthier, M. T. Reeves, X. Yu, A. S. Bradley, M. Baker, T. A. Bell, H. Rubinsztein-Dunlop, M. J. Davis, T. W. Neely, "Negative-Temperature Onsager Vortex Clusters in a Quantum Fluid", arXiv:1801.06951 (2018)

Off-Axis Cluster Transition

The *Point Vortex Model* is widely used to study turbulence in ideal two-dimensional fluids.

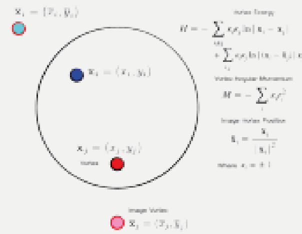

In an equilibrium state, average vortex position depends on both the energy and angular momentum of the vortices. Energy constraints tends keeps vortices clustered while angular momentum places vortices off-axis. Competition between energy and angular momentum cause clusters to move off axis at higher energy for a given angular momentum. This transition resembles a second order phase transition which can only occur at absolute negative Boltzmann temperatures.

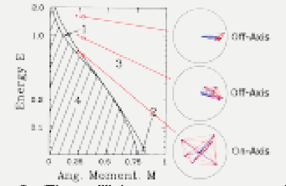

Fig. 2 - The equilibrium parameter space consists of four distinct regions with on-axis equilibria in region 1 and off-axis equilibria in region 2 (adapted from [2]). The angular momentum is proportional to the vortex distance from the centre of the trap (blue lines) whereas the energy is inversely proportional to the distances between the vortices (red lines). At higher energies this breaks symmetry and forces the vortex cluster off axis.

Experimental Results

From the vortex positions we can calculate the energy and momentum of the vortices, as well as clustering statistics, the most important of which is the average vortex position or the dipole moment [5]. Three initial vortex configurations were used see Fig. 1. On-axis d) (Red 40 runs), off-axis f) (Blue 49 runs) and two symmetrically placed clusters g) (Green 41 runs), with images taken at 250 ms steps over a 7 seconds.

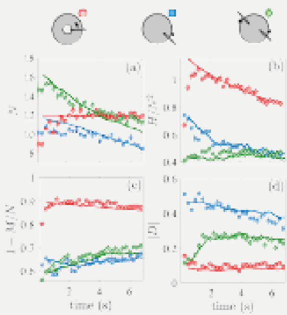

Fig. 3 - Plots of the vortex number, energy, angular momentum and dipole moment calculated from vortex position. The markers indicate experimental values while the solid lines indicate point vortex simulations

The on-axis and off-axis clusters were initially close to equilibrium see dipole moment Fig. 3 so their average position is close to constant. However the initial state with two symmetric vortex clusters starts in a symmetric non-equilibrium state and evolves into a single non-axisymmetric cluster see Fig. 3. This symmetry breaking shows that a single off-axis cluster is the equilibrium position and is quickly realised relative to the timespan of the experiment. In order to model the vortex dynamics with point vortex simulations we used an extra Brownian motion term to provide diffusion, leading to decreasing energy, angular momentum and vortex loss. This has excellent quantitative agreement with experiment, while the equilibrium cluster size and position are in agreement with mean-field theory and Monte-Carlo simulations [1, 3].

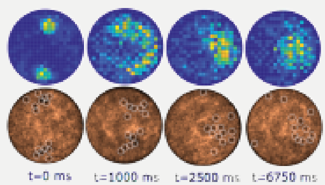

Fig. 4 - Data from the two symmetrically placed clusters (Green). The top row are histograms of vortex position. The middle row are experimental images with marked vortex positions.

These results experimentally show the long predicted symmetry breaking for vortex clusters. We also confirm that a cluster is the equilibrium position. Furthermore our results are strongly in agreement with point vortex simulations, monte-carlo simulations, and mean field theory.

Symmetry Breaking Equilibria in a Quantum Vortex Gas

Kwan Goddard Lee

Bose Einstein Condensates (BECs) behave as nearly ideal fluids, allowing many previously inaccessible fluid dynamic phenomena to be experimentally observed and explored. In particular we are interested in the behaviour of quantised vortices which, in two dimensions, tend to cluster together at high energy. This is an equilibrium state known as an Onsager Cluster. Competition between angular momentum and energy leads to spontaneous symmetry breaking, a phenomena that can only be realised at negative Boltzmann temperatures. Our results also show that a system of few vortices ~15, agree well with thermodynamical predictions.

SELF-GUIDED QUANTUM TOMOGRAPHY with QUDITS

Markus Rambach, Mahdi Qaryan, Michael Kewming, Christopher Ferrie, Andrew G. White, and Jacquiline Romero

Australian Research Council Centre of Excellence for Engineered Quantum Systems

What is Quantum State Tomography ?

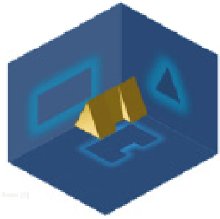

Standard Tomography vs. Self-Guided Tomography

	STANDARD QUANTUM TOMOGRAPHY	SELF-GUIDED TOMOGRAPHY
Number of required measurements	Grows exponentially	Grows Linearly
Processing time	Grows exponentially	No post-processing needed
Statistical noise	Sensitive	Robust
Measurement errors (Environmental imperfections)	Sensitive	Robust

That is how Self-Guided Tomography works

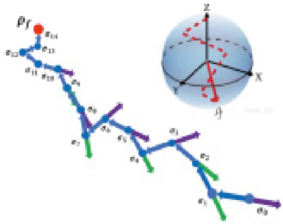

Infidelity Results; Standard Tomography vs. Self-Guided Tomography

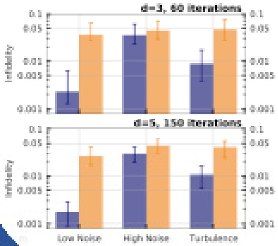

Functionality of Self-Guided Tomography in d=20

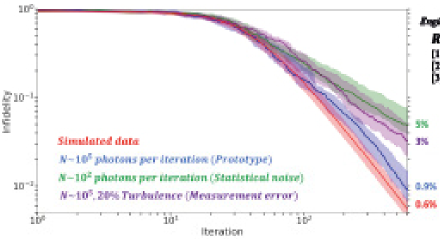

Acknowledgements

We acknowledge the ARC Centre of Excellence in Engineered Quantum Systems (EQUS) for the financial support.

References

[1] *Advances in Optics and Photonics 11.1 (2019): 67-134*
[2] *Physical review letters 113.19 (2014): 190404*
[3] *By Markus Rambach, University of Queensland*

The University of Queensland
Australia
Create Change

Australian Government
Australian Research Council

EQUS

Self-Guided Quantum Tomography with QUDITS

Mahdi Qaryan

Practical quantum communication requires high information capacity. Quantum systems with more than two levels–qudits–can provide us a rich platform for communication which results in higher information capacity. I will discuss an experimental approach that makes qudits more practical for real-world purposes. This approach named Self-guided quantum state tomography makes the procedure of tomography more feasible for higher-dimensional quantum systems.

Formation of Ultra-compact Dwarf Galaxies by Galaxy Stripping

Rebecca Mayes[1], Michael Drinkwater[1], Holger Baumgardt[1], Joel Pfeffer[2]

1. University of Queensland
2. Liverpool John Moores University

Introduction

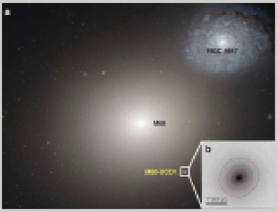

Figure 1 shows a UCD discovered in M60 [1]

Ultra-Compact Dwarf Galaxies (UCDs) are intermediate objects: larger, brighter and more massive than globular clusters but more compact than similarly luminous dwarf galaxies. Different formation scenarios suggest they may be:

1. High-mass globular clusters [2]
2. Formed from the merger of globular clusters [3]
3. The tidally stripped nuclei of dwarf galaxies [4] [5]

Tidal stripping likely produces at least some of the UCD population. However, the exact numbers of UCDs produced by tidal stripping is unknown.

In this study, we use the hydrodynamic EAGLE simulation to predict properties of UCDs formed by tidal stripping in clusters similar in mass to the Virgo cluster.

New method for finding stripped nuclei

To identify galaxies which may be stripped we search the merger trees of galaxies in clusters.

We modify EAGLE by defining the most bound star particle (MBP) of nucleated galaxies as the nucleus and tracking it through the simulation.

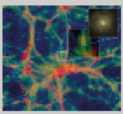

Figure 2 A slice through the EAGLE simulation [6]

The $z = 0$ positions of these MBPs could then be determined and properties derived and compared to observations of UCDs in the Virgo cluster.

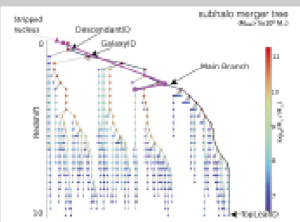

Figure 3 An example merger tree of a galaxy with the simulation modified to include a stripped nucleus. [7]

Results: Stripped nuclei locations

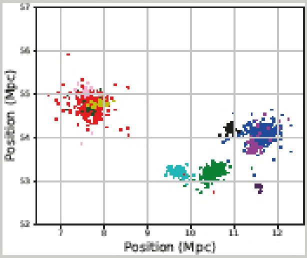

Figure 4 shows stripped nuclei for the ten most massive galaxies of the cluster in different colours. The stripped nuclei cluster around the most massive galaxies, rather than spread evenly through the cluster. If stripped nuclei are the primary source for UCD formation observed UCD distributions should also show evidence of clustering.

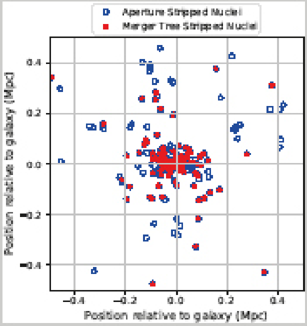

Figure 4 shows stripped nuclei clustering around the most massive galaxy in the most massive cluster. Red stars are merger-tree nuclei stripped by this galaxy. Blue points are all stripped nuclei found within a 500 kpc aperture surrounding this galaxy.

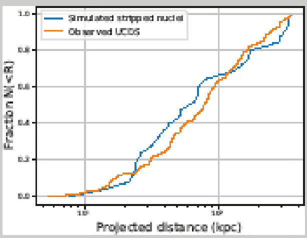

Figure 5 Cumulative distribution of $M > 1 \times 10^7$ $M_\odot$ stripped nuclei of the most massive simulated galaxy of the cluster and UCDs around M87. Applying the K-S test to these two distributions returns $p = 0.46$.

Results: Stripped nuclei numbers

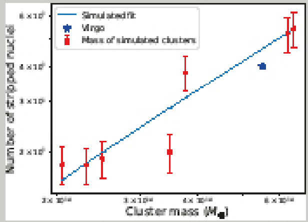

Figure 6 shows the number of $M > 1 \times 10^7$ $M_\odot$ stripped nuclei found in high mass clusters as compared to Virgo. The number-cluster mass relation is consistent with the number of observed UCDs in the Virgo Cluster (to 1 sigma).

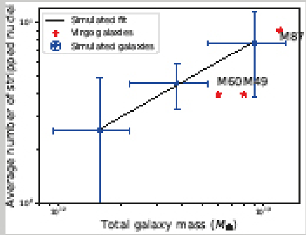

Figure 7 shows the number of $M > 1 \times 10^7$ $M_\odot$ UCDs and stripped nuclei in individual galaxies, against galaxy halo mass. All three Virgo galaxies are found within one sigma of the line of best fit

Conclusion

- Simulations show stripped dwarf galaxy nuclei cluster strongly around their host galaxies rather than being spread throughout the cluster. Observed UCDs have similar clustering patterns.
- The stripped nuclei distribution of the most massive galaxy of the simulated cluster is consistent with the distribution of UCDs around M87.
- The number of $M > 1 \times 10^7$ $M_\odot$ stripped nuclei predicted in clusters and around individual galaxies is consistent with the number of UCDs in the Virgo cluster.
- There is a high probability that UCDs form from the disruption of dwarf galaxies.

References

[1] A. C. Seth et al. A supermassive black hole in an ultra-compact dwarf galaxy. Nature, 513:398–400, September 2014.

[2] S. Mieske, M. Hilker, and I. Misgeld. The specific frequencies of ultra-compact dwarf galaxies. Astronomy and Astrophysics, 537:A3, January 2012.

[3] R. C. Brüns and P. Kroupa. A catalog of extended clusters and ultra-compact dwarf galaxies. An analysis of their parameters in early- and late-type galaxies. Astronomy and Astrophysics, 547:A65, November 2012.

[4] K. Bekki et al. Galaxy threshing and the origin of ultra-compact dwarf galaxies in the Fornax cluster. Monthly Notices of the RAS, 344:399–411, September 2003.

[5] Pfeffer J. et al. Contribution of stripped nuclear clusters to globular cluster and ultracompact dwarf galaxy populations. Monthly Notices of the Royal Astronomical Society, 444(4):3670–3683, 2014.

[6] J. Schaye et al. The EAGLE project: simulating the evolution and assembly of galaxies and their environments. Monthly Notices of the RAS, 446:521–554, January 2015.

[7] The EAGLE team. The EAGLE simulations of galaxy formation: Public release of particle data. ArXiv e-prints, June 2017.

r.mayes@uqconnect.edu.au

Formation of Ultra-compact DwarfGalaxies by Galaxy Stripping

Rebecca Mayes

This project aims to predict the numbers and distributions of Ultra-Compact Dwarf Galaxies (UCDs) formed from tidal stripping of nucleated dwarf galaxies. Tidal stripping is predicted to produce some percentage of the UCD population, however the exact numbers and distribution of UCDs that tidal stripping produces is unknown. To find the numbers and distributions of UCDs that tidal stripping produces the Eagle simulation suite is used. The Eagle simulations can model the formation of UCDs by tracing the merger trees of galaxies within a simulated cluster similar to the Virgo cluster. By designating the most bound particle of each galaxy prior to its merger in the merger tree as the nucleus, this particle can be tracked across snapshots and its position at the present day can be determined. Properties such as stellar mass, black hole mass, colour and metallicity can then be derived for the resulting UCD and compared to observations of UCDs. Thus far I have completed the process of finding the locations of most bound particles for seven massive clusters in the EAGLE simulation, and found that stripped nuclei cluster strongly around their host galaxies. I have compared the distributions of the stripped nuclei associated with simulated galaxies to the distribution of UCDs observed around massive galaxies in the Virgo cluster, and found that they are consistent. I have compared the number of stripped nuclei predicted in massive clusters and around massive galaxies to the number of UCDs in the Virgo cluster and around massive observed galaxies and found that they are also consistent.

Multiple Formation Pathways for S0s

Simon Deeley[1], Michael Drinkwater[1], Sarah Sweet[1], Jonathan Diaz[2], Kenji Bekki[2], Duncan Forbes[3], Warrick Couch[3,4] and Arianna Dolfi[3]

[1] School of Mathematics and Physics, University of Queensland, Brisbane, Queensland 4072, Australia
[2] International Centre for Radio Astronomy Research, The University of Western Australia, 35 Stirling Highway, Crawley, Western Australia, 6009, Australia
[3] Centre for Astrophysics & Supercomputing, Swinburne University, Hawthorn, VIC 3122, Australia
[4] Australian Astronomical Observatory, 105 Delhi Rd, North Ryde, NSW 2113, Australia

S0 Galaxies

S0 galaxies feature a central bulge and a smooth disk, with very little gas or star formation activity. Despite being incredibly common in the Universe, how they form, particularly in low-density environments, remains an open question.

Aim: To determine which of the proposed S0 formation pathway/s are actually occurring in the Universe

v/σ: ratio of rotational (v) to random (σ) stellar motion

Sersic Index: measure of the light profile, lower values meaning more centrally concentrated

Possible Pathways - Which one happens?

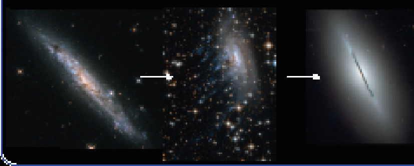

Star-forming gas removed from spiral, leaving old smooth disk

Prediction:
High v/σ
Low Sersic index

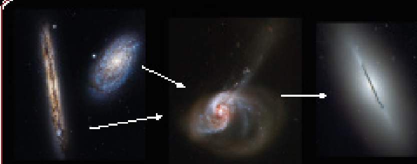

Galaxies merge to form new galaxy, disrupting spiral structure

Prediction:
Low v/σ
High Sersic index

Observations (Deeley et al. 2020)

- We use the SAMI galaxy survey to investigate the structure and kinematics of S0s
- We calculated v/σ from 2D kinematic maps and compare these to the expectations above

Structure & Rotational Support

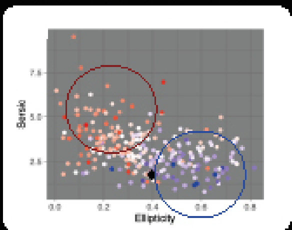

Gas-star rotational alignment

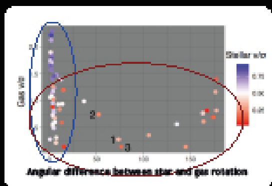

Kinematic Profiles

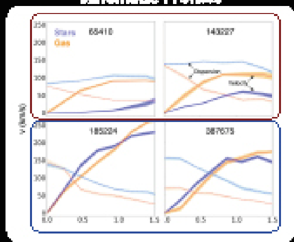

S0s circled in red have a high degree of pressure support, elliptical-like Sersic indices and misaligned gas-star kinematics, as expected for the disruptive merger pathway

S0s circled in blue have a high degree of rotational support, spiral-like Sersic indices and co-rotating gas-star kinematics, as expected for S0s forming through the more passive stripping/fading pathway

Simulations

Using the IllustrisTNG-100 cosmological simulation, we identified and tracked the formation histories of S0 galaxies, further testing if multiple formation pathways are active.

Colour and gas evolution of all S0s

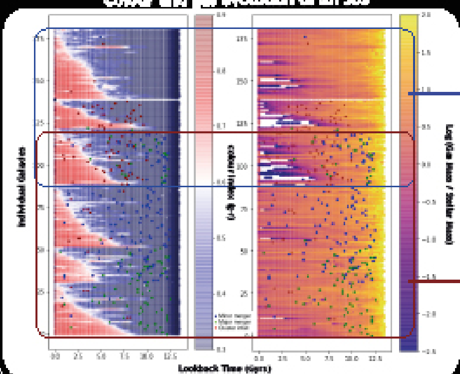

Evolution of individual S0s

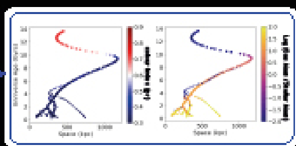

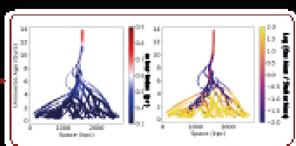

We identified multiple pathways for S0 formation, falling within two main groups (with overlap). Those in the red-boxed group have been stripped of all gas, while those in the blue group have experienced significant merger events.

Conclusions

Using both observations and simulations, we have shown that both of the main proposed formation pathways are occurring.

The final step is to calculate v/σ from the simulated galaxies and determine if they match the observational findings.

Reference:
Deeley, S., et al., 2020, MNRAS, 498, 2372

Multiple Formation Pathways for S0s

Simon Deeley

S0 (or lenticular) galaxies are very common throughout the Universe, yet how these galaxies form remains highly debated. Two main formation pathways have been proposed; the first involves the gradual fading or gas-stripping of a blue spiral galaxy, and the second involves a disruptive merger event. Here we combine both observations and simulations to identify which formation pathway is actually occurring. Our results indicate that both formation pathways are active, showing that hidden within the group of visually similar galaxies lies two very different formation histories.

What is a Quantum Shock Wave?

S. A. Simmons,[1] F. A. Bayocboc, Jr.,[1] J. C. Pillay,[1] D. Colas,[1,2] I. P. McCulloch,[1] and K. V. Kheruntsyan[1]

THE UNIVERSITY OF QUEENSLAND AUSTRALIA

[1]School of Mathematics and Physics, University of Queensland, Brisbane, Queensland 4072, Australia
[2]ARC Centre of Excellence in Future Low-Energy Electronics Technologies, University of Queensland, Brisbane, Queensland 4072, Australia

FLEET

Motivation

- What is the analogue of classical shock waves, like the morning glory cloud, in quantum fluids?
- How do they behave?
- What is their underlying physical origin?
- What role do interactions and quantum fluctuations play?

Fig 1. The morning glory roll cloud, an impressive example of a classical dispersive shock wave [1].

In the quantum realm, these structures have been observed in:

- dilute-gas Bose-Einstein condensates [2]
- rarefied plasma [3]
- intense electron beams [4]
- liquid helium [5]
- exciton polaritons [6]

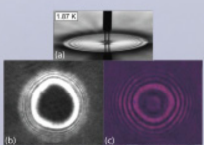

Fig 2. Dispersive shock waves in; (a) superfluid helium, (b) a Bose-Einstein condensate, (c) a Gaussian beam after passing through a non-linear optical material [1].

Whilst quantum shock waves have been observed, some of their features (including their physical origin) are not well understood.

Dispersive shock waves in expansive classical cloud rolls and in microscopic quantum fluids are both described by the same hydrodynamic type equations, but their fundamental origin is completely different!

System: Lieb-Liniger model of a one-dimensional Bose gas

Integrable Lieb-Liniger model for N bosons of mass m with repulsive pairwise contact interactions [7],

$$\hat{H} = \int dx\, \hat{\Psi}^\dagger \frac{-\hbar^2}{2m}\frac{\partial^2}{\partial x^2}\hat{\Psi} + \frac{g}{2}\int dx\, \hat{\Psi}^\dagger\hat{\Psi}^\dagger\hat{\Psi}\hat{\Psi}.$$

$\hat{\Psi}^\dagger(x)$, $\hat{\Psi}(x)$ = Bose field operators, g = interparticle interaction strength

$$\gamma_{bg} = \frac{\text{interaction energy scale}}{\text{kinetic energy scale}} = \frac{mg}{\hbar^2\rho_{bg}} \rightarrow \text{governs the interaction regime of the gas}$$

Dynamical scenario: an initial density bump expands into a non-zero background density ρ_{bg}

Ideal Gas ($\gamma_{bg} = 0$)

An initial wave function $\Psi(x,0) = \psi_{bg}(1+\beta e^{-x^2/2\sigma^2})$ evolves into a uniform potential of length L with periodic boundary conditions. In all cases, $\beta = 1$ is the height of the Gaussian bump above the constant background ψ_{bg} and $\sigma/L = 0.02$ is the width of the bump.

The time-dependent Schrodinger equation provides the solution in the ideal (non-interacting) regime,

$$i\hbar\frac{\partial}{\partial t}\Psi(x,t) = \frac{-\hbar^2}{2m}\frac{\partial^2}{\partial x^2}\Psi(x,t).$$

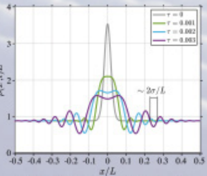

Fig 3. Single-particle probability densities at different dimensionless times $\tau = t/t_0$, where $t_0 = mL^2/\hbar$.

An analytical solution is obtainable in this case,

$$\Psi(x,t) = \psi_{bg}\left(1 + \frac{\beta\sigma}{\sqrt{\sigma^2 + i\hbar t/m}}e^{-x^2/2(\sigma^2+i\hbar t/m)}\right)$$

which can be rewritten as $\Psi(x,t) = \psi_{bg}[1 + B(x,t)e^{i\varphi(x,t)}]$ so that *the density acquires a textbook form of quantum mechanical interference,*

$$\rho(x,t) = |\Psi(x,t)|^2 = \psi_{bg}^2[1 + B^2 + 2B\cos\varphi]$$

with appropriately calculated amplitude $B(x,t)$ and phase $\varphi(x,t)$ [8].

Weak Interactions ($\gamma_{bg} \ll 1$)

Superfluid hydrodynamics provides the solution for the mean-field density $\rho(x,t)$ and velocity field $v(x,t)$ in this regime,

$$\frac{\partial\rho}{\partial t} = -\frac{\partial}{\partial x}[\rho v]$$

$$\frac{\partial v}{\partial t} = -\frac{\partial}{\partial x}\left[\frac{1}{2}v^2 + \frac{g\rho}{m} - \boxed{\frac{\hbar^2}{2m^2}\frac{1}{\sqrt{\rho}}\frac{\partial^2\sqrt{\rho}}{\partial x^2}}\right].$$

The dispersive "quantum pressure" term controls the formation of the shock wave density ripples.

If the oscillations in the interacting case remain the result of quantum interference, they will depend on the coherence of the system which is effected by,

- the interaction strength
- quantum fluctuations
- thermal fluctuations

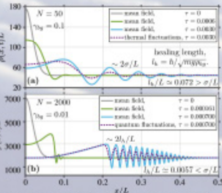

Fig 4. Zero temperature mean-field density profiles (solid lines), with examples showing the effect of quantum fluctuations ($T = 0$) and thermal fluctuations ($\bar{T} = T/T_d = 0.32$, $T_d = \hbar^2\rho_{bg}^2/2mk_B$).

Quantum and thermal fluctuations reduce the coherence length of the system → amplitude of interference contrast decreases.

Strong Interactions ($\gamma_{bg} \gtrsim 1$)

At stronger interaction strengths the coherence length of the system reduces until it reaches the size of the interparticle separation as $\gamma_{bg} \rightarrow \infty$ [9]. Accordingly, the interference contrast (density ripples) disappears.

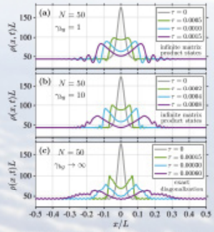

Fig 5. Probability density profiles of an intermediately, strongly, and infinitely interacting Bose gas; where all quantum effects have been included.

Conclusions

- A quantum shock wave is a dispersive shock wave.
- The trailing edge of the shock wave travels at the speed of sound in the fluid.
- The fundamental mechanism behind their formation is quantum mechanical self-interference; a density bump interferes with its own background upon expanding into it.
- The density ripples can be considered interference fringes who's contrast depends on the coherence of the system.

References

[1] G. El & M. Hoefer, Physica D 333, 11 (2016)
[2] M. Hoefer *et al.*, Phys. Rev. A 74, 023623 (2006)
[3] R. Taylor *et al.*, Phys. Rev. Lett. 24, 206 (1970)
[4] Y. Mo *et al.*, Phys. Rev. Lett. 110, 084802 (2013)
[5] E. Rolley *et al.*, Physica B 394, 46 (2007)
[6] L. Dominici *et al.*, Nature Communications 6, 1 (2015)
[7] E. Lieb & W. Liniger, Phys. Rev. 130, 1605 (1963)
[8] S. Simmons *et al.*, arXiv:2006.15326 (2020)
[9] M. Girardeau, Journal of Mathematical Physics 1, 516 (1960)

What is a Quantum Shock Wave?

Steven Simmons

Shock waves are examples of the far-from-equilibrium behaviour of matter; they are ubiquitous in nature, yet the underlying microscopic mechanisms behind their formation are not well understood. Here, we study the dynamics of dispersive quantum shock waves in a one-dimensional Bose gas, and show that the oscillatory train forming from a local density bump expanding into a uniform background is a result of quantum mechanical self-interference. The amplitude of oscillations, i.e., the interference contrast, decreases with the increase of both the temperature of the gas and the interaction strength due to the reduced phase coherence length. Furthermore, we show that vacuum and thermal fluctuations can significantly wash out the interference contrast, seen in the mean-field approaches, due to shot-to-shot fluctuations in the position of interference fringes around the mean.

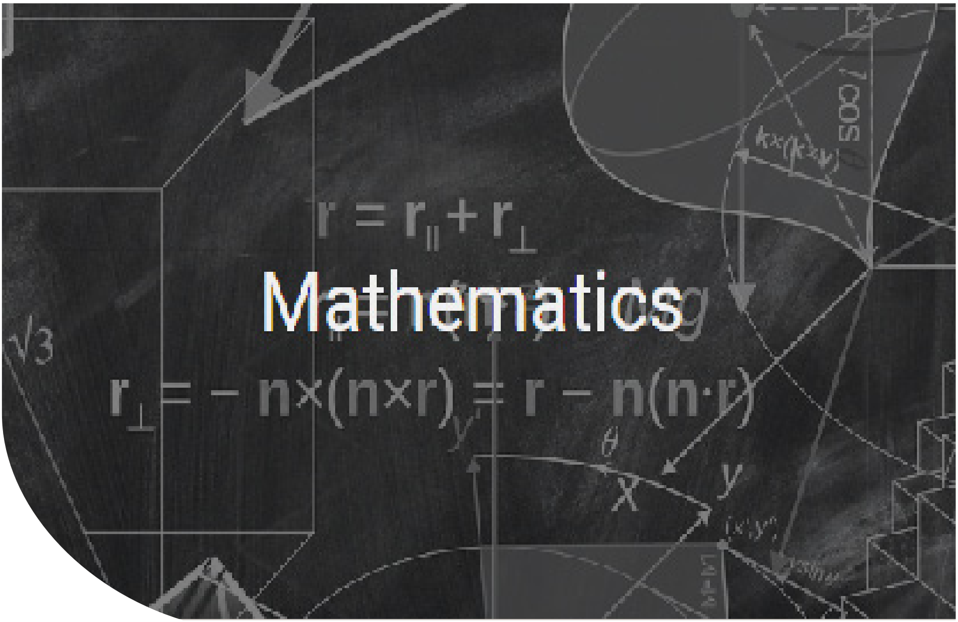

Mathematics

THE UNIVERSITY OF QUEENSLAND
AUSTRALIA

COLOUR LIE ALGEBRAS STRUCTURE WITH A VIEW TO APPLICATIONS

Alhanouf M. Almutairi

PhD Supervisors: Dr. Phillip Isaac and Prof. Mark Gould

School of Mathematics and Physics, The University of Queensland, St Lucia, Australia

Introduction

Due to the prevalence of colour Lie algebras in the context of integrable models, an ongoing area of interest for research is the explicit developing of the structure of these objects. The goal of this research is to develop and study certain algebra embeddings, particularly embeddings of colour Lie algebras within quantum groups at roots of unity.
To this end, the research specifically aims to undertake the following:

- As a specific prototype, determine the existence of $\mathbb{Z}_2 \times \mathbb{Z}_2$- graded colour variants of the Lie algebra $\mathfrak{gl}(n)$ inside the quantum group $U_q(\mathfrak{gl}(n))$ in the limit as $q \to -1$.
- Study the embeddings of $\mathbb{Z}_2 \times \mathbb{Z}_2$-graded colour within the q-Schrödinger algebra in the limit $q \to -1$.

$\mathbb{Z}_2 \times \mathbb{Z}_2$- graded Lie colour algebras

Following [5,6], let $\tilde{\mathfrak{g}}$ be a $\mathbb{Z}_2 \times \mathbb{Z}_2$-graded vector space over $\mathbb{C}$, that decomposes as

$$\tilde{\mathfrak{g}} = \tilde{\mathfrak{g}}_{(0,0)} \oplus \tilde{\mathfrak{g}}_{(1,1)} \oplus \tilde{\mathfrak{g}}_{(1,0)} \oplus \tilde{\mathfrak{g}}_{(0,1)}.$$

For a homogeneous element $x_a \in \tilde{\mathfrak{g}}_a$, $a = (0,0), (1,1), (1,0)$, or $(0,1)$, the *degree* of x_a is $\tilde{d}(x_a) = a$. $\tilde{\mathfrak{g}}$ is endowed with a bilinear product $[\![\cdot,\cdot]\!] : \tilde{\mathfrak{g}} \otimes \tilde{\mathfrak{g}} \to \tilde{\mathfrak{g}}$ that preserves grading, i.e. if $x \in \tilde{\mathfrak{g}}_{\tilde{d}(x)}$, $y \in \tilde{\mathfrak{g}}_{\tilde{d}(y)}$, then $[\![x,y]\!] \in \tilde{\mathfrak{g}}_{\tilde{d}(x)+\tilde{d}(y)}$ (componentwise addition mod 2).

$$[\![x,y]\!] = -(-1)^{\tilde{d}(x)\cdot\tilde{d}(y)}[\![y,x]\!], \text{ (graded antisymmetry)}$$

$$[\![[\![x,y]\!],z]\!] = [\![x,[\![y,z]\!]]\!] - (-1)^{\tilde{d}(x)\cdot\tilde{d}(y)}[\![y,[\![x,z]\!]]\!], \text{ (graded Jacobi identity).}$$

$\tilde{d}(x) = (x_1, x_2)$, $\tilde{d}(y) = (y_1, y_2) \Rightarrow \tilde{d}(x)\cdot\tilde{d}(y) = x_1y_1 + x_2y_2$ mod 2.

The main object of our study in this research is the $\mathbb{Z}_2 \times \mathbb{Z}_2$-graded general linear superalgebra $\mathfrak{gl}(m_1, m_2|n_1, n_2)$, where the labels m_1, m_2, n_1 and n_2 are non-negative integers. As in the $\mathbb{Z}_2$-graded case, a convenient basis is the standard one comprising (homogeneous) elementary matrices $\tilde{E}_{ij}$ with 1 in the entry of row i, column j and 0 elsewhere. Using the graded index notation introduced in [6]

$$\tilde{d}_i = \begin{cases} (0,0);\ i = 1,\dots,m_1 \\ (1,1);\ i = m_1+1,\dots,m_1+m_2 \\ (1,0);\ i = m_1+m_2+1,\dots,m_1+m_2+n_1 \\ (0,1);\ i = m_1+m_2+n_1+1,\dots,m_1+m_2+n_1+n_2. \end{cases}$$

It is a homogeneous matrix with degree given by $\tilde{d}_{ij} := \tilde{d}(\tilde{E}_{ij}) = \tilde{d}_i + \tilde{d}_j$ mod $(2,2)$. The $\mathbb{Z}_2 \times \mathbb{Z}_2$-graded Lie product is given as follows,

$$[\![\tilde{E}_{ij}, \tilde{E}_{k\ell}]\!] = \delta_{jk}\tilde{E}_{i\ell} - (-1)^{\tilde{d}_{ij}\cdot\tilde{d}_{k\ell}}\delta_{i\ell}\tilde{E}_{kj},$$

and the universal enveloping algebra $U(\mathfrak{gl}(m_1, m_2|n_1, n_2))$ is the unital associative algebra subject to the relations

$$\tilde{E}_{ij}\tilde{E}_{k\ell} - (-1)^{\tilde{d}_{ij}\cdot\tilde{d}_{k\ell}}\tilde{E}_{k\ell}\tilde{E}_{ij} = \delta_{jk}\tilde{E}_{i\ell} - (-1)^{\tilde{d}_{ij}\cdot\tilde{d}_{k\ell}}\delta_{i\ell}\tilde{E}_{kj}.$$

Recently, Isaac et al [4] constructed operators inside an algebraic extension of the enveloping algebra of Lie superalgebra $\mathfrak{gl}(m|n)$ that realise $\mathfrak{gl}(m_1, m_2|n_1, n_2)$, with $m = m_1 + m_2$ and $n = n_1 + n_2$.

Quantum group $U_q(\mathfrak{gl}(n))$

The quantum group $U_q(\mathfrak{gl}(n))$ over a complex field $\mathbb{C}$ is defined as a unital associative algebra generated by $\{h_i, h_n, e_i, f_i\}$, $\{i = 1, ..., n-1\}$ and the relations

$$[h_i, h_j] = 0 = [h_n, e_j] = [h_n, f_j], \quad [h_i, e_j] = a_{ij}e_j, \quad [h_i, f_j] = -a_{ij}f_j$$

$$[e_i, f_j] = \delta_{ij}\frac{q^{h_i} - q^{-h_i}}{q - q^{-1}},$$

where (a_{ij}) denotes the Cartan matrix of type $\mathfrak{sl}(n)$. In $U_q(\mathfrak{gl}(n))$, introduce generators

$$E_i = e_i q^{h_i},$$
$$F_i = q^{-h_i} f_i.$$

Embedding of $U(\mathfrak{gl}(n_1, n_2|n_3, n_4))$ in $U_{-1}(\mathfrak{gl}(n))$

To demonstrate how the embedding has been constructed, we exhibit the theory in the context of the integer partitions. A partition of an integer n up to length 4 is a representation of n as a sum of integers ≥ 1, considering the order of terms of this sum. We denote the colour algebra associated with these ordered partitions by $\mathfrak{gl}(n_1, n_2|n_3, n_4)$ such that $n_1 + n_2 + n_3 + n_4 = n$. Now, we need to count all the partitions of a positive integer $\mathfrak{gl}(n)$ up to length 4, where the order is important and no more than one of the labels n_1, n_2, n_3, n_4 is zero. The importance of the order is to distinguish, for example, structures such as $\mathfrak{gl}(2,0|1,1)$ and $\mathfrak{gl}(0,2|1,1)$. This can happen by considering all the cases of the isomorphism since these isomorphisms will reduce the counts by one. In the following, we have included all the isomorphic cases,

Proposition

(1) $\mathfrak{gl}(n_1, 0|n_3, n_4) \cong \mathfrak{gl}(0, n_2|n_3, n_4)$,

(2) $\mathfrak{gl}(n_1, n_2|n_3, 0) \cong \mathfrak{gl}(n_1, n_2|0, n_4)$,

(3) $\mathfrak{gl}(n_1, n_2|n_3, n_4) \cong \mathfrak{gl}(n_2, n_1|n_3, n_4)$,

(4) $\mathfrak{gl}(n_1, n_2|n_3, n_4) \cong \mathfrak{gl}(n_1, n_2|n_4, n_3)$.

Corollary:

$$\mathfrak{gl}(n_1, n_2|n_3, n_4) \cong \mathfrak{gl}(n_2, n_1|n_4, n_3).$$

We have applied these isomorphisms to reduce the number of distinct examples and we obtain the generating sequence of $\mathfrak{gl}(n)$, $n = 1, 2, 3, 4, 5, ...$ as the following:

$$0, 0, 2, 5, 10, 17, 26, 38, 52, ... \tag{1}$$

We are now in a position to find a generating function of the sequence in (1) and we consider two separate cases. Firstly, when $n = 2k, k = 1, 2, 3, ...,$, the total sum of all the possibilities is

$$d_1(n) = \frac{n^3 + 9n^2 - 22n}{24}.$$

Secondly, in the case when $n = 2k + 1,\ k = 0, 1, 2, ...$, where k is positive integer

$$d_2(n) = \frac{n^3 + 9n^2 - 25n + 15}{24}.$$

A q-Schrödinger algebra $U_q(\mathfrak{g}_{1,\frac{1}{2}})$

The algebra $U_q(\mathfrak{g}_{1,\frac{1}{2}})$ has the nontrivial q-commutation relations [3]

$$[D, P_t] = -2P_t, \quad [D, K] = 2K, \quad [P_x, K] = G\, q^{-D}, \quad [P_t, K] = [D]_q,$$
$$[D, G] = G, \quad [P_x, D] = P_x, \quad P_t\, P_x - q^{-1} P_x\, P_t = 0,$$
$$P_t\, G - q\, G\, P_t = P_x, \quad P_x\, G - q^{-1}\, G\, P_x = 0,$$

where q-number notations:

$$[a]_q = \frac{q^a - q^{-a}}{q - q^{-1}}.$$

So far we have determined the embeddings of $\mathbb{Z}_2 \times \mathbb{Z}_2$- graded colour superalgebras within q-Schrödinger algebra. When $q \to -1$, let

$$\tilde{G} = G, \qquad \tilde{P}_t = P_t(-1)^D, \qquad \tilde{D} = D,$$
$$\tilde{K} = (-1)^{-D}K, \qquad \tilde{P}_x = P_x(-1)^D.$$

We construct the $\mathbb{Z}_2 \times \mathbb{Z}_2$- graded algebra by the idea same as [1,2], that is, by transforming bosonic operators into fermionic ones. The assignment of $\mathbb{Z}_2 \times \mathbb{Z}_2$ degree is given by

$$\begin{array}{ll} (0,0): & \tilde{D},\ \tilde{N},\ \tilde{E},\ \tilde{F} \\ (1,0): & \tilde{P}_x,\ \tilde{B} \\ (0,1): & \tilde{K},\ \tilde{P}_t,\ \tilde{W} \\ (1,1): & \tilde{G} \end{array}$$

The $\mathbb{Z}_2 \times \mathbb{Z}_2$ degree of $\tilde{K},\ \tilde{P}_x,\ \tilde{P}_t$, and $\tilde{G}$ forces us to introduce new elements:

$$\{\tilde{P}_x, \tilde{P}_x\} = \tilde{N}, \quad \{\tilde{P}_t, \tilde{P}_t\} = \tilde{E}, \quad \{\tilde{K}, \tilde{K}\} = \tilde{F},$$
$$\{\tilde{G}, \tilde{K}\} = \tilde{B}, \quad \{\tilde{P}_x, \tilde{G}\} = \tilde{W}.$$

Future work

- finite-dimensional q-conformal Galilei algebras
- $\mathbb{Z}_2 \times \mathbb{Z}_2$-graded colour embeddings of q-conformal Galilei algebras in the limit $q \to -1$
- Recast the known $\mathbb{Z}_2 \times \mathbb{Z}_2$-graded symmetry of the Lévy-Leblond equations
- Representations theory of the associated quantum group

References

(1) N. Aizawa, A. Kuznetsova, H. Tanaka and F. Toppan, In: S. Duarte et al. (eds.) Phys. Math. Asps. Syms. 79, (2017).
(2) N. Aizawa, Adv. Appl. Clifford Algebras 28, 28 (2018).
(3) V. K. Dobrev, H. D. Doebner and C. Mrugalla, J. Phys. A: Math. Gen. 29, 5909 (1996).
(4) P. S. Isaac, N.I. Stoilova and J. V. d. Jeugt, J. Math. Phys. 61, 011702 (2020).
(5) V. Rittenberg and D. Wyler, Nucl. Phys. B 139, 189 (1978).
(6) V.N. Tolstoy, Phys. Part. Nuclei Lett. 11, 933 (2014).

Colour Lie algebras structure with a view to applications

Alhanouf Mubarak B Almutairi

We discuss the limit of q as a root of unity of q- deformations corresponding to a semisimple Lie algebra gl(n) and non-semisimple Schrödinger algebra, and consider the presence of colour Lie algebras occurring as subalgebras in this limit. This will largely be a survey of the relevant literature, and a presentation of some preliminary results relating to certain colour Lie algebras.

The Evolution of Menopause

Anthia Le
anthia.le@uqconnect.edu.au
Supervisors: Dr. Zoltan Neufeld (UQ), A/Prof. Peter Kim (USyd) & Prof. Mark Gould (UQ)

Background: **In the Plio-Pleistocene period (ca. 2 million years ago), our African ancestors experienced an ecological shift from forest to savannah. When food sources became harder to access by juveniles, several social and behavioural adaptations separated humans from our close primate relatives. In particular, human adult lifespans include a post-menopausal life stage.**

Model 1: Female-Only

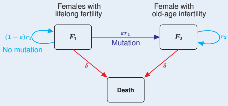

A system of ordinary differential equations where r_1 and r_2 are the female reproductive contribution

$$\frac{dF_1}{dt} = (1-\varepsilon)r_1F_1 - \delta F_1,$$
$$\frac{dF_2}{dt} = \varepsilon r_1F_1 + r_2F_2 - \delta F_2.$$

Simulation

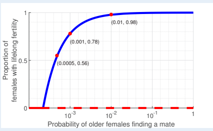

- If a small number of older females mate, lifelong fertility will be the dominant trait.

Problem: Is menopause a product of male mate selection?

Morton et al. suggested human females evolved old-age infertility through ancestral males forgoing mating with older females. As their agent-based model is difficult to analyse, we propose the following system of ordinary differential equations.

We consider four populations:

Females with lifelong fertility F_1 | **Females with old-age infertility F_2**

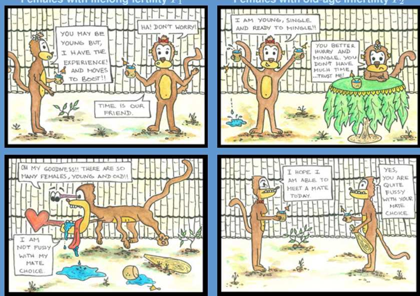

Unfussy males M_1; mates with all females | **Fussy males M_2**; mates with young females

Model 2: Two-Sex

Explicitly including males where similarly, $s_1(t)$ and $s_2(t)$ are the male reproductive contribution

$$\frac{dF_1}{dt} = (1-\varepsilon)r_1(t)F_1 - \delta F_1,$$
$$\frac{dF_2}{dt} = \varepsilon r_1(t)F_1 + r_2(t)F_2 - \delta F_2,$$
$$\frac{dM_1}{dt} = s_1(t)\frac{M_1}{M_1+M_2} - \delta M_1,$$
$$\frac{dM_2}{dt} = s_2(t)\frac{M_2}{M_1+M_2} - \delta M_2.$$

Simulation

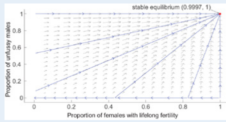

- Females with lifelong fertility and unfussy males will make up a majority of the population.
- Unfussy and fussy males cannot co-exist because M_1's willingness to mate with older females gives them a strong evolutionary advantage.

Conclusion: **It is unsustainable and evolutionarily inferior for males to limit their mating preference. Consider the Grandmother Hypothesis: older females subsidise juveniles as the environment shifted.**

What if menopause arose from older females choosing to stop reproducing?

References

[1] Richard A. Morton, Jonathan R. Stone, and Rama S. Singh. Mate choice and the origin of menopause. *PLOS Computational Biology*, 9(6):1–8, 06 2013.

[2] Kristen Hawkes and James E Coxworth. Grandmothers and the evolution of human longevity: A review of findings and future directions. *Evolutionary Anthropology: Issues, News, and Reviews*, 22(6):294–302, 2013.

Acknowledgements

A special thank you to distinguished Professor Kristen Hawkes for her input throughout the modelling process.

The Evolution of Menopause

Anthia Le

When we examine the life history of humans against our close primate relatives , we see that human adult lifespans include a post-menopausal life stage. This leads to the question, "how did human females evolve to have old-age infertility?" Morton et al. suggested that ancestral male mating choices, particularly forgoing mating with older females, was the driving force behind the evolution of menopause. As their agent-based model is difficult to analyse, we propose an analogous system of ordinary differential equations (ODE) to examine their conclusions. Our conclusions contradict that of Morton et al., as we find that even the slightest deviation from an exclusive mating preference for younger females would counteract the evolution of menopause.

THE UNIVERSITY OF QUEENSLAND
AUSTRALIA

Sachdev-Ye-Kitaev Model and Time-Average Procedure

Ming Chen, Yao-Zhong Zhang

Through the time-average procedure, this poster proposes a new perspective to treat the SYK model. In this interpretation, the SYK model can be taken as a special case of this procedure and its effective theory can naturally preserve a conformal property.

The Sachdev-Ye-Kitaev (SYK) model describes an 1-dimensional (1D) spin-liquid system [1][2][3], its hamiltonian in the model's physical 1D Euclidean space reads [1][3][6],

$$H = H_0 + H_{\text{int}} = -\frac{1}{2}\chi_j \frac{d}{d\tau}\chi_j - \sum_{1\leq j<k<l<m\leq N_s} \mathcal{J}_{jklm}\chi_j\chi_k\chi_l\chi_m, \quad (1)$$

where χ denotes the Majorana fermions (MFs) with Hermitian conjugation $\chi^\dagger = \chi$ and the indices j, k, l, m represent 4 sites picked from N_s sites, indicating quartic interactions at a time in each term of H_{int}. The quenched energy-dimensional "coupling coefficients" $\mathcal{J}_{jklm}$ are all randomly taken from the following Gaussian probability distribution, with its mean and variance respectively as $\mu = \overline{\mathcal{J}_{jklm}} = 0$ and $\sigma^2 = \overline{\mathcal{J}^2_{jklm}} = \frac{J^2 3!}{N_s^3}$,

$$\mathcal{P}(\mathcal{J}_{jklm}) \sim \frac{1}{\sigma\sqrt{2\pi}} exp\Big(-\frac{1}{2}\frac{(\mathcal{J}_{jklm}-\mu)^2}{\sigma^2}\Big), \quad (2)$$

The model's replica-free effective action can be achieved after integrating out the MFs [1][3][9]. Then the Dyson equations can be calculated through the saddle points of the effective action in the infrared (IR) limit [8][3],

$$\begin{cases} G(\tau,\tau') = \frac{1}{-\partial_\tau - \Sigma(\tau,\tau')} \overset{\text{frequency space}}{=\!=\!=\!=\!=\!=\!=} \frac{1}{-i\omega - \Sigma(i\omega)}; \\ \Sigma(\tau,\tau') = J^2 G^3(\tau,\tau'), \end{cases} \quad (3)$$

where G is the bilocal field denoting MF 2-point Green functions ($G(\tau,\tau') = \sum_i^{N_s}\chi_i(\tau)\chi_i(\tau')$) and Σ is the auxiliary bilocal field denoting the fermion self-energy ($\Sigma(\tau,\tau') = J^2G^3(\tau,\tau')$).

The frequency will tend to zero in such IR limit, so that the "$i\omega$" term can be ignored. Then the Dyson equations display an emergent time-reparameterization symmetry as $\tau \mapsto f(\tau)$, which shows a conformal property of SYK's solution because it preserves diffeomorphisms and Weyl invariance under certain conformal maps, like $\tau \mapsto f(\tau) \sim e^{i\phi(\tau)}$. For such a conformal symmetry, we can use $SL(2,\mathbb{R})$ group to fit the conformal transformations [10].

Based on the above arguments, it is reasonable to form a power law decay of τ at long time in the IR limit [6]: $G(\tau,\tau') \sim \frac{1}{\sqrt{T}}$ with $T = |\tau - \tau'|$. We then assume the squared Green functions as follows,

$$G^2(\tau,\tau') = \begin{cases} \frac{1}{T}, & -\frac{T}{2} \leq \tau;\tau' \leq \frac{T}{2}; \\ 0, & \text{otherwise}, \end{cases} \quad (4)$$

with the underlying identity: $\mathbf{1} = G^2(\tau,\tau')\cdot T = \frac{1}{T}\int_{-T/2}^{T/2} G^2(\tau,\tau')d\tau d\tau'$.

This resembles the time-average procedure for a statistical system wherein the macrostates can be bridged with microstates by $g = \frac{1}{T}\int_{-T}^{T} g(t)dt$, where g is certain macroscopic quantity and $g(t)$ the microstates. The system's equilibrium can be approached by integrating out the time to infinity.

Similarly, we now take the following equation as a system's equilibrium in the form of time-averaging,

$$\langle G^2(\tau,\tau')\rangle = \lim_{T\to\infty}\frac{1}{T}\iint_{-T/2}^{T/2} G^2(\tau,\tau')d\tau d\tau'. \quad (5)$$

From the definition in Eq.(4), T and $(\tau;\tau')$ form a rectangle with fixed area. Such a property can be reserved through T-transformations on $(\tau;\tau')$, that is, we can always translate $(\tau;\tau')$ till it lies within a finite region $[-\frac{1}{2},\frac{1}{2}]$.

Under such a T-transformation, the limit $T\to\infty$ can be absorbed into region $[-\frac{1}{2},\frac{1}{2}]$. Together with the reciprocal of T which is the S-transformations [11], the integration over $(\tau;\tau')$ will be invariant under the modular transformations which take the form of $SL(2,\mathbb{R})$ symmetry group [12]. As a result, the integration over $(\tau;\tau')$ is actually the integration over the fundamental domain of $SL(2,\mathbb{R})$,

$$\{SL(2,\mathbb{R})\} \mapsto \big\{|T|\geq 1, \quad \tau;\tau' \in [-\frac{1}{2},\frac{1}{2}]\big\}. \quad (6)$$

By now, Eq.(5) can be simplified,

$$\langle G^2(\tau,\tau')\rangle = \frac{1}{T}\int_{\{SL(2,\mathbb{R})\}} G^2(\tau,\tau')d\tau d\tau'. \quad (7)$$

To be noted, the "bi-time" in $G^2(\tau,\tau')$ are actually on equal footing, thus the Euclidean space is a natural choice. Meanwhile, the Euclidean $G^2(\tau,\tau')$ is holomorphic in times ($G(\tau,\tau') \sim\chi(\tau)\chi(\tau')$). Therefore, the time-averaging formula takes the similar form with the action in the SYK model,

$$\langle G^2(\tau,\tau')\rangle = \frac{1}{T}\int_{\{SL(2,\mathbb{R})\}}[\chi(\tau)\chi(\tau')][\chi(\tau)\chi(\tau')]d\tau d\tau'. \quad (8)$$

To relate this formula closer with the SYK model, a coupling coefficient (with dimension $[\mathcal{J}] = 1$) can be equipped by replacing the prefactor $\frac{1}{T}$, which indicates the interactions among those χ symbols,

$$\langle G^2(\tau,\tau')\rangle = \mathcal{J}_{1234}\int_{\{SL(2,\mathbb{R})\}}[\chi_1(\tau)\chi_2(\tau')][\chi_3(\tau)\chi_4(\tau')]d\tau d\tau'. \quad (9)$$

If we take the system's macrostates in equilibrium as potential (interactions) with kinetic ignored, then Eq.(9) is the general expression of system's action. And the coupling coefficient can be further equipped through certain probability distribution with suitable mean and variance, we can specify Eq.(9) as,

$$S_{\text{int}} \sim \sum_{j,k,l,m}^{N_s}\int_{\{SL(2,\mathbb{R})\}}\mathcal{J}_{jklm}\chi_j(\tau)\chi_k(\tau')\chi_l(\tau)\chi_m(\tau')d\tau d\tau', \quad (10)$$

where $\mathcal{J}$ takes the zero mean and variance $\sigma^2 = \overline{\mathcal{J}^2_{jklm}} \sim J^2$ with dimension $[J] = 1$.

Spectacularly, χ symbols acquire an anomalous dimension $\frac{1}{4}$, which is exactly the same as the MFs in the SYK model [5].

After $\mathcal{J}$-distribution average, the action leads to another square of quadruple χ symbols with the help of replica method. Then the effective action of this formula can be arrived at through successive Hubbard-Stratonovich transformations [6] or an auxiliary δ-identity [3].

Thus, the SYK model can be seen as special cases of time-average procedure. Specially, through the interpretation of the SYK model in this procedure, the effective theory of the SYK model can naturally preserves the conformal symmetry. Furthermore, there is no reason to exclude other form of $G(\tau,\tau')$, as long as it is holomorphic in its parameters. Therefore, it leaves an ample region for more choices, e.g., the general formula of the SYK model with arbitrary even number of MFs [4].

[1] A.Kitaev, "*A simple model of quantum holography*", *talks at Kavli Institute for Theoretical Physics*, Santa Barbara, U.S.A, (2015), http://online.kitp.ucsb.edu/online/entangled15/kitaev/, http://online.kitp.ucsb.edu/online/entangled15/kitaev2/.

[2] A.Kitaev, "*A Toy Quantum Black Hole*", *talk in Brown Physics Colloquium*, Brown University Department of Physics, (2017).

[3] A.Kitaev and S.J.Suh, "*The soft mode in the Sachdev-Ye-Kitaev model and its gravity dual*", *J. High Energy Phys.*, **05**: 183 (2018).

[4] J.Maldacena and D.Stanford, "*Remarks on the Sachdev-Ye-Kitaev model*", *Phys. Rev. D.*, **94**: 106002 (2016).

[5] J.Polchinski and V.Rosenhaus, "*The spectrum in the Sachdev-Ye-Kitaev model* ", *J. High Energy Phys.*, **04**: 001 (2016).

[6] S.Sachdev, "*Beskenstein-Hawking Entropy and Strange Metals* ", *Phys. Rev. X.*, **5**: 041025 (2015), arXiv: 1506.05111v4 [hep-th] (2015).

[7] S.Sachdev and J.W.Ye, "*Gapless Spin-Fluid Ground State in a Random Quantum Heisenberg Magnet* ", *Phys. Rev. Lett.*, **70**: 21 (1993).

[8] D.Bagrets, A.Altland and A.Kamenev, "*Sachdev-Ye-Kitaev model as Liouville quantum mechanics*", *Nucl. Phys. B*, **911**: 191-205 (2016).

[9] A.Kitaev, "*Notes on $\widetilde{SL}(2,\mathbb{R})$ representations* ", arXiv: 1711.08169v2 [hep-th] (2018).

[10] C.Vafa and E.Witten, "*A strong coupling test of S-duality* ", *Nucl. Phys. B*, **431**: 3-77 (1994).

[11] David Tong, "*String Theory*", University of Cambridge Part III Mathematical Tripos, UK, (arXiv: 0908.0333v3 [hep-th]) (2012).

Sachdev-Ye-Kitaev Model and Time-Average Procedure

Ming Chen

Through the time-average procedure, this poster proposes a new perspective to treat the SYK model. In this interpretation, the SYK model can be taken as a special case of this procedure and its effective theory can naturally preserve a conformal property.

NOTE: Ming is currently offshore due to the COVID-19 travel restrictions and hasn't been able to return to Australia since the start of the year.

He won't at the event, but he has created a video to guide you through his poster. You can find this via the link below or scanning the QR Code.

https://bit.ly/347D22m

Classification and stability analysis of travelling wave solutions for collective cell migration in an epithelial layer.

THE UNIVERSITY OF QUEENSLAND
AUSTRALIA

Nizhum Rahman
Program: PhD   Candidature Status: Confirmed
School of Mathematics and Physics
Advisors: Dr. Dietmar Oelz, Dr. Zoltan Neufeld & Prof. Alpha Yap

Introduction:
A travelling wave is a wave that travels in a particular direction, with a fixed shape.

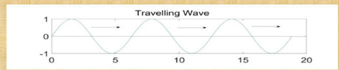

Epithelial cell: Epithelial cell is a type of cell that lines the surfaces of our body.

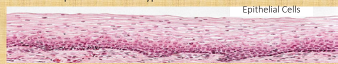

It has been found that cell polarisation and migratory directionality propagates within a sheet of cells like a travelling wave. We calculate all possible wave speeds and their stability.

Methods:
The following 1D model for cell polarisation and migration in a epithelial layer has been proposed [1]:

$$\frac{\partial \rho}{\partial t}+\frac{\partial(\rho M_n(a))}{\partial x}-\frac{\partial}{\partial x}\left(\frac{k\,\partial \rho}{\rho^2 \partial x}\right)=0$$

$$\frac{\partial a}{\partial t}+\left(M_n(a)-k\frac{1\,\partial \rho}{\rho^3 dx}\right)\left(\frac{\partial a}{\partial x}-1\right)+a=0\,.$$

Where $\rho(x)$ is the cell density, $a(\mathrm{x})$ is the cell polarity.
For finding travelling waves we transfer these equations in moving coordinate as $z=s-xt$, where 's' is the travelling wave of polarity.

Preliminary Result:
The travelling wave for polarisation due to departing cell sheet.

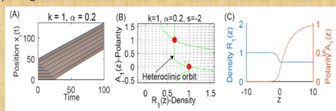

Result-1:
We obtain different types of travelling waves due to departing or colliding cell sheets. To obtain these we apply two different transformations:
$T1\colon (R(z),A(z),s)\rightarrow(\bar R(\bar z),\bar A(\bar z),\bar s)$,
where $\bar A=A, \frac{1}{\bar R}+\frac{1}{R}=2\,,\ \bar z=\int_0^z(1-2\,\bar R)d\bar z$ and $\bar s=-s$
$T1\colon \big(\rho(x,t),a(x,t)\big)\rightarrow\big(\bar\rho(\bar x,\bar t),\bar a(\bar x,\bar t)\big)$,
where $\bar t=t, \bar a=1-a\,, \bar x=t-x, \bar v=1-v$ and $\bar\rho=\rho$

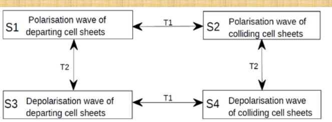

Decreasing of polarisation is referred as depolarisation.

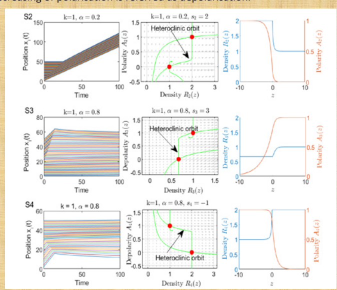

Result-2:
Stability: Mathematically, a travelling wave solution is said to be stable if small perturbations or disturbances of the wave do not alter its form. After linearizing the system and writing it as an eigenvalue problem: $(\mathcal{L}-I\lambda)\begin{pmatrix}\delta\rho\\ \delta v\\ \delta a\end{pmatrix}=0$. We convert the eigenvalue problem into a system of first order ODEs:

$$\begin{pmatrix}\delta\rho'\\ \delta v'\\ \delta a'\end{pmatrix}=A(z,\lambda)\begin{pmatrix}\delta\rho\\ \delta v\\ \delta a\end{pmatrix}, \text{ where } A(z,\lambda)=\begin{pmatrix}\frac{3R'}{R} & \frac{-R^3}{k} & \frac{M'R^3}{k}\\ \frac{2R's-R^2\lambda}{R^3} & \frac{-R'}{R}-\frac{Rs}{k} & \frac{M'Rs}{k}\\ 0 & \frac{(A'-1)R}{s} & \frac{R(\lambda+1)}{s}\end{pmatrix}.$$

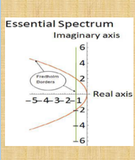

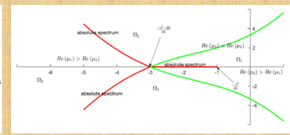

As the Fredholm border touches the imaginary axis of the complex plane, so we study the absolute spectrum [2]. In the exponentially weighted space, the absolute spectrum is on the left side of the complex plane, so our travelling waves are essentially stable [2].

Result-3:
Evans Function: We investigate the point spectrum of the operator $\mathcal{L}$ by using the Evans function. The Evans function $D(\lambda)$ represents the determinant of unstable eigenvectors of A_- (at $z=-\infty$) and stable eigenvectors of A_+ (at $z=\infty$), both propagated to $z=0$ by the operator $\mathcal{L}$.

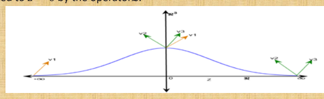

$D(\lambda)=0$ if, and only if λ is in the point spectrum of $\mathcal{L}$.

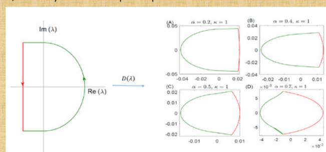

We apply the argument principle as it states that, the winding number around the origin is equal to the number of zeros in a closed contour [3].

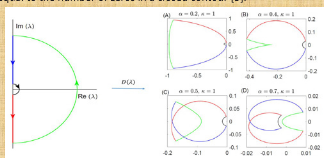

We see that the winding number (point spectrum) is zero unless the origin of the complex plane is included, so our travelling waves solution are linearly stable.

Applications:
A better understanding of the mechanisms that allow to control polarisation and depolarisation of migrating epithelial cells has the potential to contribute to the understanding of tumour biology, wound healing and to be used in the bioengineering of tissue implants.

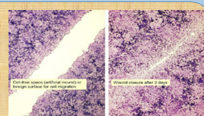

https://www.dartsch-scientific.com/en/wundheilung-zellregeneration/

References:
1. Dietmar Oelz, Hamid Khataee, Andras Czirok, and Zoltan Neufeld, "Polarization wave at the onset of collective cell migration" , Physical Review E ,2019.
2. Björn Sandstede, "Stability of Travelling Waves" , Volume 2, 2002, Pages 983-1055, ELSEVIER.
3. Matthew H. Chan, Peter S. Kim, Robert Marangell, "Stability of travelling waves in a *Wolbachia* invasion". *Discrete & Continuous dynamical Systems - B*, 2018.

Classification and stability analysis of travelling wave solutions for collective cell migration in an epithelial layer

Nizhum Rahman

We identify travelling wave solutions arising in a model for collective cell migration in epithelial layers. We investigate their stability, most notably we analyse the essential and absolute spectra and we apply the Evans function to investigate the point spectrum.

The Dial-A-Ride Problem: Combining Dantzig-Wolfe and Benders Decomposition

Yannik Rist
School of Maths and Physics
yannik.rist@uqconnect.edu.au

The Dial-A-Ride Problem (DARP)

- Similar to the Travelling Salesman Problem (must visit all locations, no subtours, minimise travel cost).
- Multiple capacitated vehicles (capacity constraints).
- Pickup and Delivery location pairs, must visit each pickup before its delivery (pairing and precedence constraints).
- Time constraints: time windows at locations and ride times between pickup and delivery.
- Well studied; existing work with both Combinatorial Benders Decomposition and Branch-and-Price approaches. The latter is considered state-of-the-art.

Dantzig-Wolfe Decomposition/Branch-and-Price

- Formulation with strong, "composite" decision variables which contain most of the constraints.
- Provides strong lower bounds on objective which accelerates the Branch-and-Bound algorithm.
- Direct enumeration of variables is intractible; generate variables as-needed to prove optimality.
- DARP: Variables for each possible DARP route.

Combinatorial Benders Decomposition

- Replace weak constraints in a problem with a large pool of stronger constraints.
- Direct inclusion of all constraints is intractible; relax problem and add constraints (Benders Cuts) as-needed to ensure feasibility.
- If the underlying model has weak lower bounds, Combinatorial Benders Decomposition will not improve them by much.
- DARP: Benders Cuts for capacity, precedence and pairing.

DARP Models

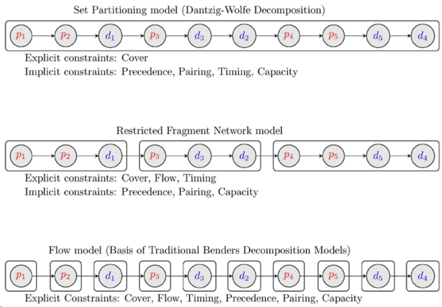

Hybrid Approach for the DARP (Restricted Fragment Network)

- Group pickups and deliveries together into *restricted fragments*. Use variables indexed by restricted fragments.
- Like Branch-and-Price, these contain some of the constraints (see above).
- Smaller objects than routes; less numerous and can enumerate them directly.
- Handle remaining timing constraints with Combinatorial Benders Decomposition.
- Stronger lower bounds than traditional Benders models.
- Speedup of 1-2 orders of magnitude compared to state-of-the-art Branch-and-Price.

Comparing Objective Bounds

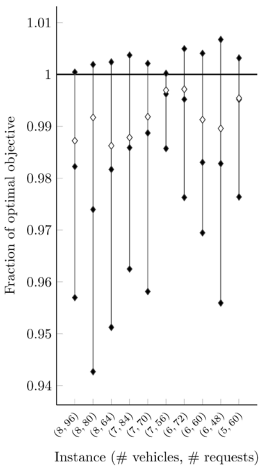

Black points: our approach; from bottom: Initial lower bound, initial lower bound with valid inequalities and initial upper bound.

White points: Initial lower bound using Branch-and-Price with valid inequalities.

Time windows: bounds on arrival times.

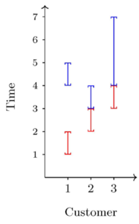

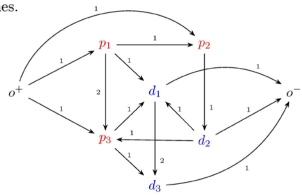

Physical network: nodes are locations, edges are labelled with travel times/costs.

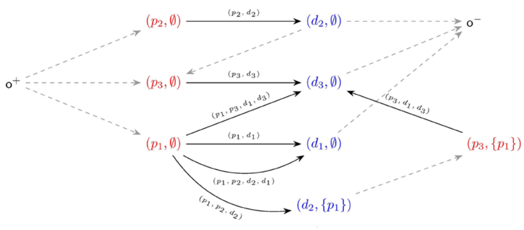

Restricted Fragment Network: nodes consist of a location and the load currently onboard the vehicle. Solid edges are fragments, dashed edges link depots and fragments together.

The Dial-A-Ride Problem: Combining Dantzig-Wolfe and Benders Decomposition

Yannik Rist

Benders Decomposition and Dantzig-Wolfe Decomposition, in the form of Branch-and-Price, are two well-established techniques for solving difficult mixed integer programs. Branch-and-Price methods have dominated much of the literature on vehicle routing problems, which play an important role in health care, supply chain management and public transport. By using a hybrid approach which combines the two techniques, it is possible to exploit advantages of both methods while avoiding their worst drawbacks. The new approach has proven highly successful for the Dial-A-Ride problem, a type of vehicle routing problem.

A new representation for the Landau-de Gennes energy of nematic liquid crystals

Zhewen(Joe) Feng
z.feng@uq.edu.au

Principal Advisor: A/Prof Min-Chun Hong
Associate Advisor: Prof. Joseph Grotowski

THE UNIVERSITY OF QUEENSLAND
AUSTRALIA

Introduction

◇ Liquid crystals are common around us: soap, some cell membranes and your smart phone.

"Liquid crystals are beautiful and mysterious."

– Nobel Prize Laureate Pierre-Gilles de Gennes

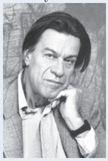

Fig. 1

◇ A celebrated theory: the Landau-de Gennes (LdG) theory.
◇ The LdG formulation (2 parameters) is generalizable: Longa et al. (1987) gave a 22-parameter LdG energy density (c.f. [1]).
◇ The simplest phase of such complex fluid is known as nematics.
◇ Based on the molecular shape: uniaxial and biaxial nematics.

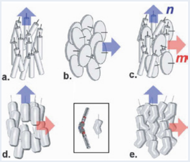

Fig. 2

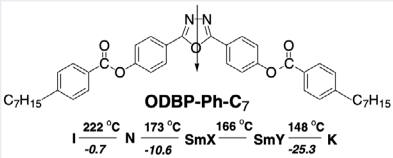

Fig. 3

◇ For uniaxial nematics, to agree with the verified Oseen-Frank model, Dickmann (1995) derived a (4-parameter) LdG energy density that is widely accepted and studied (c.f. [1]):

$$f_E(Q,\nabla Q) = \frac{L_1}{2}|\nabla Q|^2 + \frac{L_2}{2}\frac{\partial Q_{ij}}{\partial x_j}\frac{\partial Q_{ik}}{\partial x_k} + \frac{L_3}{2}\frac{\partial Q_{ik}}{\partial x_j}\frac{\partial Q_{ij}}{\partial x_k} + \frac{L_4}{2}Q_{lk}\frac{\partial Q_{ij}}{\partial x_l}\frac{\partial Q_{ij}}{\partial x_k}, \quad (1)$$

(elastic density part)

$$f_B(Q) = -\frac{a}{2}\operatorname{tr}(Q^2) - \frac{b}{3}\operatorname{tr}(Q^3) + \frac{c}{4}\left[\operatorname{tr}(Q^2)\right]^2. \quad (2)$$

(bulk density part)

(summing over repeated indices)

The unknown $Q \in S_0 := \{Q \in \mathbb{M}^{3\times 3} : Q^T = Q, \operatorname{tr} Q = 0\}$. The L_i are the material constants.

A coercivity problem: For $\Omega \in \mathbb{R}^3$ and $Q \in W^{1,2}(\Omega; S_0)$, Ball and Majumdar (2010) proved that

$$E_{LdG} := \int_\Omega \Big(f_E(Q,\nabla Q) + f_B(Q)\Big)\,dx$$

does not satisfy a coercivity condition for $L_4 \neq 0$. This means that

existence of minimizers for E_{LdG} cannot be guaranteed in $W^{1,2}(\Omega; S_0)$.

A new representation

◇ For uniaxial nematic liquid crystals, we [2] discover that (a, b and c are material constants)

$$Q_{lk}\frac{\partial Q_{ij}}{\partial x_l}\frac{\partial Q_{ij}}{\partial x_k} = \frac{3}{s_+}\Big(Q_{ln}\frac{\partial Q_{ij}}{\partial x_l}\Big)\Big(Q_{kn}\frac{\partial Q_{ij}}{\partial x_k}\Big) - \frac{2s_+}{3}|\nabla Q|^2, \qquad s_+ := \frac{b+\sqrt{b^2+24ac}}{4c}.$$

◇ Then for $Q \in S_* := \{Q \in S_0 : Q = s_+(u\otimes u - \frac{1}{3}I), u \in S^2\}$, we propose the following

$$E(Q;\Omega) = \int_\Omega f_{E,1}(Q,\nabla Q)\,dx = \int_\Omega \Big(\frac{L_1}{2} - \frac{s_+ L_4}{3}\Big)|\nabla Q|^2 + \frac{L_2}{2}\frac{\partial Q_{ij}}{\partial x_j}\frac{\partial Q_{ik}}{\partial x_k}\,dx$$
$$+ \int_\Omega \frac{L_3}{2}\frac{\partial Q_{ik}}{\partial x_j}\frac{\partial Q_{ij}}{\partial x_k} + \frac{3L_4}{2s_+}Q_{ln}Q_{kn}\frac{\partial Q_{ij}}{\partial x_l}\frac{\partial Q_{ij}}{\partial x_k}\,dx. \quad (3)$$

Note that $f_{E,1}$ is equivalent to $f_E(Q,\nabla Q)$ and inclusive of Longa's extensive representation.

◇ An answer to the coercivity problem is $L_2 \geq 0$, $L_4 \geq 0$, $L_1 - |L_3| - \frac{2s_+}{3}L_4 > 0$.

Relaxed Q-tensor and its limit

◇ The Euler-Lagrange (EL) equation for our new energy functional is restricted that $Q \in S_*$. Similarly to the Ginzburg-landau approximation, we consider a relaxed energy functional

$$E_L(Q_L;\Omega) = \int_\Omega \Big(f_{E,1}(Q_L,\nabla Q_L) + \frac{1}{L}\big(f_B(Q_L) - \min_{Q_L\in S_0} f_B(Q_L)\big)\Big)\,dx, \quad Q_L \in W^{1,2}(\Omega; S_0).$$

◇ For a given uniaxial boundary, we prove that there exist minimizers $Q_L \in W^{1,2}(\Omega; S_0)$ **converge strongly**, as $L \to 0$, to a minimizer $Q \in S_*$ for $E(Q;\Omega)$ that is partially regular.

◇ Assume $\lim_{L\to 0}\frac{1}{L}\int_\Omega (f_B(Q_L) - \min_{Q_L\in S_0} f_B(Q_L))\,dx = 0$, through rotations and projections one can show the strong limit of a weak solution Q_L to EL(E_L) **solves** EL(E) in the weak sense.

Results

Joint with A/Prof Min-Chun Hong, we [3]:

• propose a new form of the Landau-de Gennes' and verify the physics relavence;

• achieve the best constant assumption on L_i by rotations (equivlent to Ericksen's condition);

• derive a special type (uniaxial) of the Euler-Lagrange equation for $E(Q;\Omega)$;

• prove the existence of minimizers Q_L and show its convergence to a minimizer Q of $E(Q;\Omega)$;

• prove the limit of weak solutions Q_L to solves EL(E) (under suitable assumptions).

Discussion

The new form $E(Q;\Omega)$ opens up opportunities to study coupled Q-tensor flow problems. In the existing literature:

Majumdar and Zarnescu [4] initiated mathematical analysis on the so call one-constant approximation by considering $L_2 = L_3 = L_4 = 0$.

Paicu and Zarnescu (2011) first studied the coupled Navier-Stokes and Q-tensor system.

Over years of development, researchers (c.f. [1]) improve assumptions to $L_4 = 0$, or $|Q|_{t=0}$ is sufficiently small. The general case where $L_4 \neq 0$ remains open.

In the recent work with Hong and Mei, we [3] proved **maximal time smooth** convergence:

Ginzburg-Landau → Ericksen-Leslie's.

Based on the techniques in [3] and observation in [1] and [2], **what can we say about**

the coupled relaxed Q-tensor flow →
the coupled uniaxial Q-tensor flow?

What about the numerical simulations for the coupled relaxed Q-tensor flow?

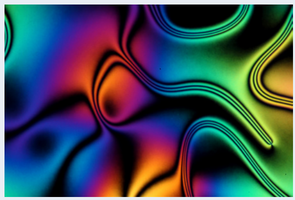

Fig. 4

References

[1] J. M. Ball. Mathematics and liquid crystals. *Molecular Crystals and Liquid Crystals*, 647(1):1–27, 2017.

[2] Z. Feng and M.-C. Hong. A new representation for the landau-de gennes energy of nematic liquid crystals. *Preprint, arXiv:2007.11144*, pages 1–32, 2020.

[3] Z. Feng, M.-C. Hong, and Y. Mei. Convergence of the ginzburg-landau approximation for the ericksen-leslie system. *SIAM J. Math. Anal.*, 52:481–523, 2020.

[4] A. Majumdar and A. Zarnescu. Landau-de gennes theory of nematic liquid crystals: the oseen-frank limit and beyond. *Arch. Ration. Mech. Anal.*, 196:227–280, 2010.

Fig. 1: Photo from the Nobel Foundation archive. [Accessed 9 Oct. 2020].

Fig. 2 & 3 L. A. Madsen and T. J. Dingemans and M. Nakata and E.T. Samulski. Thermotropic biaxial nematic liquid crystals. *Phys. Rev. Lett.* ,92, 2004.

Fig. 4: Lavrentovich, O. (n.d.). Polarization Microscope Image of Liquid Crystals (Image 4). [image] Available at: https://bit.ly/3jQLk42 [Accessed 9 Oct. 2020]

A new representation for the Landau-de Gennes energy of nematic liquid crystals

Zhewen Feng

In 1971, Nobel Prize Laureate Pierre-Gilles de Gennes proposed a theory to study liquid crystals known as the Landau-de Gennes theory. For the simplest phase of liquid crystals: nematics, Ball-Majumdar in 2010 proved that the Landau-de Gennes energy functional does not satisfy a coercivity condition, which causes a problem in mathematics to establish existence of energy minimizers. To solve this problem, we propose a new Landau-de Gennes energy, which is equivalent to the original for uniaxial nematic \$Q\$-tensors. Similarly to the work of Majumdar-Zarnescu in 2010, we prove existence and convergence of minimizers for the new Landau-de Gennes energy and discuss potential directions on liquid crystal flow problems.

CRICOS Provider 00025B

School of Mathematics and Physics

smp.uq.edu.au/physics
smp.uq.edu.au/mathematics

THE UNIVERSITY OF QUEENSLAND
AUSTRALIA

CREATE CHANGE